AD 738 061

INFLUENCE OF MICROSTRUCTURE
ON FRACTURE PROPAGATION IN ROCK

by

R. G. Hoagland
G. T. Hahn, Principal Investigator
A. R. Rosenfield
R. Simon
G. D. Nicholson

January, 1972

INFLUENCE OF MICROSTRUCTURE
ON FRACTURE PROPAGATION IN ROCK

by

R. G. Hoagland
G. T. Hahn, Principal Investigator
A. R. Rosenfield
R. Simon
G. D. Nicholson

FINAL REPORT

on

INFLUENCE OF MICROSTRUCTURE
ON FRACTURE PROPAGATION IN ROCK

by

R. G. Hoagland
G. T. Hahn, Principal Investigator
A. R. Rosenfield
R. Simon
G. D. Nicholson

January, 1972

to

BUREAU OF MINES
Twin Cities Research Center
Mr. George Savanick, Project Engineer, 612-725-4597
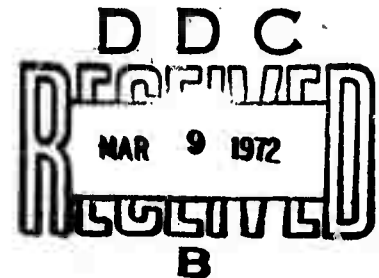
Contract No. H0210006

BATTELLE
Columbus Laboratories
505 King Avenue
Columbus, Ohio 43201

DDC

MAR 9 1972

B

DOCUMENT CONTROL DATA - R & D

(Security classification of title, body of abstract and indexing annotation must be entered when the overall report is classified)

1. ORIGINATING ACTIVITY *(Corporate author)*	2a. REPORT SECURITY CLASSIFICATION
Battelle, Columbus Laboratories	Unclassified
	2b. GROUP

3. REPORT TITLE

Influence of Microstructure on Fracture Propagation in Rock

4. DESCRIPTIVE NOTES *(Type of report and inclusive dates)*

Final Report, 18 December, 1970 to 18 December, 1

5. AUTHOR(S) *(First name, middle initial, last name)*

Richard G. Hoagland   Alan R. Rosenfield   G. D. Nicholson
George T. Hahn   Ralph Simon

6. REPORT DATE	7a. TOTAL NO. OF PAGES	7b. NO. OF REFS
January, 1972		

8a. CONTRACT OR GRANT NO	9a. ORIGINATOR'S REPORT NUMBER(S)
H0210006	
b. PROJECT NO. ARPA Order No. 1579	-
Amendment No. 2	
c. Program Code No. 1F10	9b. OTHER REPORT NO(S) *(Any other numbers that may be assigned this report)*
d.	-

10. DISTRIBUTION STATEMENT

Unlimited

11. SUPPLEMENTARY NOTES	12. SPONSORING MILITARY ACTIVITY
	Advanced Research Projects Agency

13. ABSTRACT

This report describes the results of research to correlate the fracture resistance with microstructural features of Salem limestone and Berea sandstone. Tests were conducted on wedge-loaded double-cantilever-beam specimens containing machined slot as crack starters. The fracture resistance of Salem limestone measured in terms of R, the energy dissipated per unit area of projected surface, was found to increase in the initial stage of crack extension but finally reached a constant value which was strongly dependent on crack orientation with respect to the bedding plane. For this limestone R ranges from about 50 joules $/m^2$ to 230 joules/m^2. The sandstone which is a softer and more compliant rock exhibited similar fracture behavior while the R values ranged from 465 joules/m^2 to 1580 joules/m^2. In addition, tests in liquid nitrogen which were aimed at eliminating plastic deformation in the rocks during fracture showed little difference in R for the limestone but a substantial reduction in R for the sandstone which, in the latter case, may be caused by differential thermal expansion between the quartz grains and the calcite cement. Acoustic emissions were detected in both rocks at very early stages in the tests indicating the occurrence of microcracking near the initial slot tip at low loads. The mode of fracture and the fracture path in both materials was identified by fractography over a broad range of magnifications. The evidence gained from this work strongly points to the existence of an extensive array of microcracks produced in a region surrounding the main crack tip and which advances with it. The energy dissipated in fracturing of rock is associated with the creation of the large amount of surface area contained in this microcrack array. This picture provides a self-consistent explanation for the puzzling discrepancy between the measured tensile strength of rocks and the strengths predicted from measured R values.

DD FORM 1473
NOV 65

14. KEY WORDS	LINK A		LINK B		LINK C	
	ROLE	WT	ROLE	WT	ROLE	WT
Rock Mechanics						
Rock Fracture						
Fracture Mechanics						
Microstructure						
Fractography						
Microcracking						

TABLE OF CONTENTS

ABSTRACT

This report describes the results of research to correlate the
fracture resistance with microstructural features of Salem limestone and
Berea sandstone. Tests were conducted on wedge-loaded double-cantilever-beam
specimens containing machined slots as crack starters. The fracture resistance
of Salem limestone measured in terms of R, the energy dissipated per unit area
of projected surface, was found to increase in the initial stage of crack ex-
tention but finally reached a constant value which was strongly dependent on
crack orientation with respect to the bedding plane. For this limestone R
ranges from about 50 joules/m^2 to 230 joules/m^2. The sandstone which is a
softer and more compliant rock exhibited similar fracture behavior while the R
values ranged from 465 joules/m^2 to 1580 joules/m^2. In addition, tests in
liquid nitrogen which were aimed at eliminating plastic deformation in the
rocks during fracture showed little difference in R for the limestone but a
substantial reduction in R for the sandstone which, in the latter case, may be
caused by differential thermal expansion between the quartz grains and the cal-
cite cement. Acoustic emissions were detected in both rocks at very early
stages in the tests indicating the occurrence of microcracking near the initial
slot tip at low loads. The mode of fracture and the fracture path in both
materials was identified by fractography over a broad range of magnifications.
The evidence gained from this work strongly points to the existence of an
extensive array of microcracks produced in a region surrounding the main crack
tip and which advances with it. The energy dissipated in fracturing of rock is
associated with the creation of the large amount of surface area contained in
this microcrack array. This picture provides a self-consistent explanation for
the puzzling discrepancy between the measured tensile strength of rocks and the
strengths predicted from measured R values.

i

FINAL REPORT

on

INFLUENCE OF MICROSTRUCTURE
ON FRACTURE PROPAGATION IN ROCK

by

R. G. Hoagland
G. T. Hahn, Principal Investigator
A. R. Rosenfield
R. Simon
G. D. Nicholson

INTRODUCTION

There are a number of problems which arise in developing relations between the fracture behavior of rocks and their microstructure. Among these are:

(a) Variability: The composition and microstructure of even the most common rock types are usually highly variable. Hence, mechanical property data obtained from small laboratory specimens cannot be safely applied in the field if one disregards the possible scatter of the data due to microstructural variations.

(b) High Fracture Energies: It is often observed that the mechanical properties of rocks are considerably different from those of the individual components of the rock. This is particularly true in regard to the response to a tensile stress. The energy dissipated in propagating a crack in rocks is typically much greater than is consumed for the single crystals of its constituents.

(c) <u>Strengths of Smooth Bars</u>: When the energy dissipated in propagating a large crack is used to predict tensile strengths of smooth specimens by means of the Griffith theory, the predictions are very poor, the predicted strengths greatly overestimating the measured strength. One is, therefore, faced with the puzzling result that rocks are apparently much tougher (capable of dissipating more energy) when they contain a large flaw than when they contain a small one.

(d) <u>Size Effect</u>: There is often a significant size effect since the behavior of small-scale laboratory specimens or models may not compare well with the behavior of large in situ rock masses. Therefore, to ensure that a laboratory test is to provide reliable information it is necessary to recognize the important microstuctural features and their dimensions and to scale the test specimens accordingly.[1]*

(e) <u>Comparison with Other Brittle Materials</u>: Rocks can be considered as a class of naturally occurring polycrystalline, polyphase ceramics. Any explanation of the strength and toughness of one class of material should be relevant to the other class. A comparison of properties taken from the literature is shown in Table I. Note that the ceramics have markedly higher unnotched properties while the notch

---

* References are given on page 55.

TABLE I. COMPARISON BETWEEN MECHANICAL PROPERTIES OF ROCKS AND CERAMICS

	Elastic Modulus, GN/m^2	Smooth-Bar Fracture Strength, MN/m^2	Fracture Energy, R, J/m^2	Surface Energy, γ, J/m^2
Ceramics				
Al_2O_3	280-400[4]	150-350[5]	30-110[2,5]	1[3]
Si_3N_4	125-175[6]	100-275[6]	8-12[6]	-
MgO	350[7]	100-250[7]	30[7]	2[7]
Rocks				
Various Sandstones	2-3[8]	0.3-8[8]	20-275[8]	0.5[9]
Various Limestones	11-33[8]	1.8-5[8]	15-85[8]	0.5[9]

toughnesses, R, are comparable. In fact, if average values were used instead of extreme values in Table I, the rocks would be found to be tougher than the ceramics, reversing the unnotched behavior.

The large values of fracture energy of rock are of particular interest. Perkins and Bartlett[8] examined this problem and suggested that plastic deformation occurs at the tip of a crack in rocks, in a fashion similar to metals. This process can dissipate large amounts of energy and, if it occurs in rocks, can account for the difference in toughness between a rock and its constituents. An alternative interpretation has been offered by Moavenzadeh and Kuguel[10] based on their work on concrete. They suggest that the energy dissipated per unit crack area formed is no greater in rocks than in its individual constituents but only appears greater because large amounts of area are generated by microcracks* in regions adjacent to the main fracture. This view has also been recently supported by Friedman, et al[11] from work on two limestones, sandstones, and a quartzite. This latter interpretation is also strongly supported by the results presented in this report.

This report describes research aimed at overcoming these problems. To this end, the past year's work aimed at a detailed description of the failure behavior of two sedimentary rock types: Salem limestone and Berea sandstone. The approach conbined the measurement of R, the energy dissipated in fracture, with high resolution fractography and petrography of broken rock surfaces and the material adjacent to the fracture, and with acoustic detection of microcrack formation.

---

* Also called microfractures and en-echelon microcracking.

EXPERIMENTAL PROCEDURE

The energy dissipation rates for crack extension in the limestone and sandstone were measured by means of the double-cantilever-beam (DCB) test specimen and loading arrangement shown in Figure 1. The specimen dimensions were 1.6 x 7.6 x 17.8 cm with a slot tipped with a 0.4-mm-wide sawcut placed to facilitate starting a crack having the desired orientation relative to the bedding plane. Prior to testing, the specimens were baked at 110°C in order to minimize the possible effects of differences in moisture content from one specimen to another. A few specimens were tested after a 12-hour immersion in tap water. To measure the growth of the crack a parallel array of conductive lines was placed on each specimen. The electrical resistance of the array was monitored during testing and, as the crack severed the lines, the corresponding resistance change revealed the crack-tip location. Because of the extreme brittleness of the rock, it was difficult to find a conductive material sufficiently brittle so that the strip would fail reproducibly the instant the crack in the rock passed underneath. Lines drawn on the surface with a lead pencil were found to be more reliable than either silver paint or a number of vapor deposited metals, although some uncertainty in the crack length measurements remained.

Loads were applied to the test specimens by forcing a wedge between a pair of steel pins located on either side of the specimen. Typical test records of the load applied to the wedge and the resulting crack opening displacement and crack growth are shown in Figure 2. The testing arrangement favors stable crack extension when the starting notch is a sharp crack, and unstable crack propagation when the starting notch is blunted.[12]
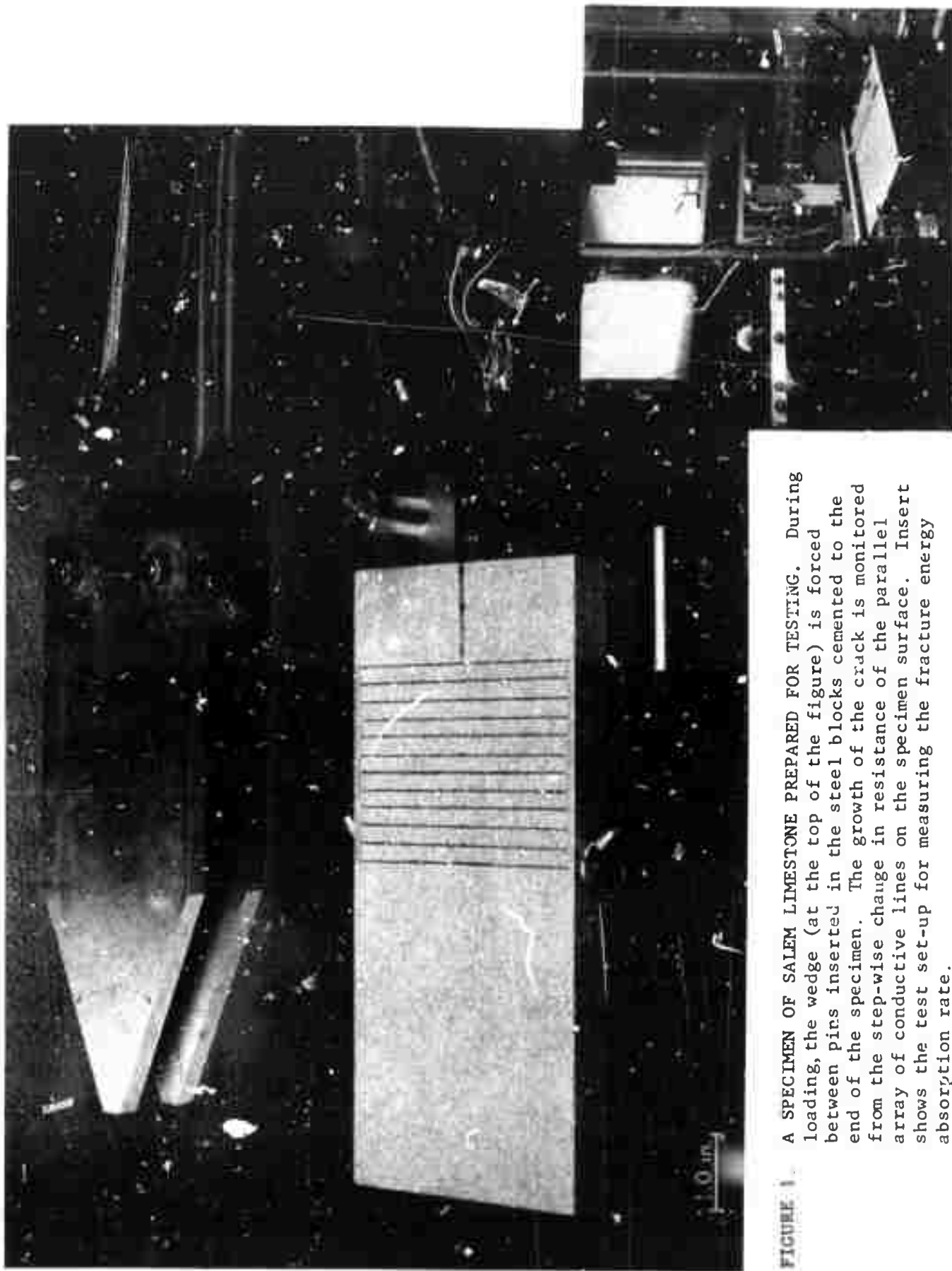
FIGURE 1. A SPECIMEN OF SALEM LIMESTONE PREPARED FOR TESTING. During loading, the wedge (at the top of the figure) is forced between pins inserted in the steel blocks cemented to the end of the specimen. The growth of the crack is monitored from the step-wise change in resistance of the parallel array of conductive lines on the specimen surface. Insert shows the test set-up for measuring the fracture energy absorption rate.
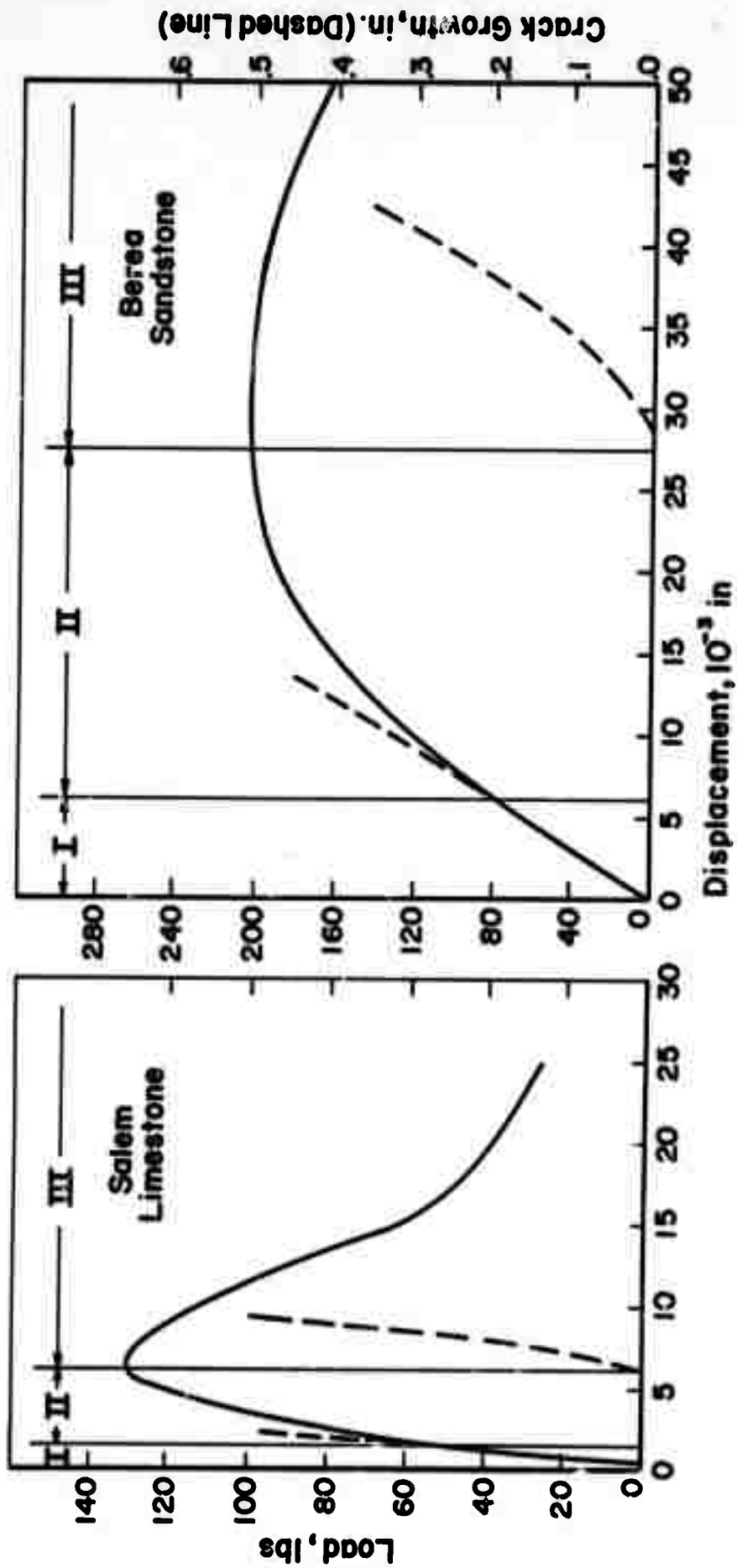
6

FIGURE 2. A TYPICAL LOAD-DISPLACEMENT-RECORD CRACK LENGTH FROM A WEDGE-LOADED DCB TEST. In the initial part of the record the crack has not yet begun to grow as indicated by the linear relation between the load and displacement. In the latter part, the load is gradually decreasing as the crack extends at a more or less constant rate.

The fracture energy dissipation rate, R, defined as the energy irreversibly consumed per unit area of crack extension, is derived from this test by way of the following energy balance:

$$R = \frac{d}{dA} (W-U) \tag{1}$$

where dW represents the work done by the testing machine during an increase of the crack area by dA and dU is the corresponding change in strain energy in the specimen. Equation (1) applies to the case where the crack is growing slowly and, therefore, the kinetic energy in the system is negligible. An analysis based on Equation (1) has been developed at Battelle which allows R to be computed from either the load-displacement record or from measured displacements and crack lengths. Details of this analysis are given in Appendix A. By convention, R is based on the projected surface area:

$$dA = bda \tag{2}$$

where b is the specimen thickness and a is the crack length. As shown in the next section, the actual crack surface is highly irregular, and the true surface area is larger than assumed in calculating R. This is an important consideration in interpreting the results of these tests.

The calculation of R from the load-displacement record depends on E, Young's modulus. The value of E employed for the limestone was determined from the slope (compliance) of the load-displacement record for a DCB specimen containing a crack of known length and ϕ, the modulus independent compliance derived from elasticity theory (see Equation (A6) in Appendix A). The ratio of these two quantities gives the value of E as

1.6×10^{11} dynes/cm^2 (2.3×10^6 psi). This value compares quite well with the zero stress value obtained from uniaxial compression data by Hardy and Kim[13] on similar material. The elastic modulus applied to the sandstone data is 7×10^{10} dynes/cm^2 (1×10^6 psi), slightly lower than the geo-pressure value of La Mori[14]. Because the sandstone exhibits a greater degree of non-linearity (in tension) this modulus is difficult to define exactly. These effects and their implication in terms of a fracture model for these materials are discussed later.

Acoustic emissions accompanying the wedge loading were monitored in a number of experiments. The emissions were detected by attaching piezo-electric crystals to the specimen surface. The crystals were acoustically coupled to the specimen by means of a viscous resin. The crystals have a resonant frequency of 150 kHz and, therefore, it is this frequency of acoustic pulses which is most sensitively detected. In tests monitoring acoustic emissions, the specimens were placed on a rubber pad on the loading platen and teflon sheets were used between the wedge and pins. These precautions were aimed at minimizing the stray noise from specimen-platen contact or from sliding of the wedge along the pin. Tests on uncracked specimens showed that these precautions were effective, and, therefore, acoustic pulses registered by the recording equipment during an actual test originate in the bulk of the specimen, presumably in the region of high stress surrounding the slot tip.

The crack path and microstructural features of the fracture surface were examined in detail in both materials. These examinations involved con-ventional optical (reflection) microscopy, scanning electron microscopy, transmission electron microscopy of Pt-C shadowed replicas, and optical (transmission) microscopy of thin slices.

EXPERIMENTAL RESULTS

Load-Displacement Crack-Length Measurements

The load displacement records for both the limestone and the sandstone can be divided into 3 regions, as shown in Figure 2. In Region I, the load-displacement record is more or less linear consistent with elastic behavior. In Region II the record then becomes increasingly nonlinear as a result of inelastic behavior in the region of high stresses surrounding the notch.

Typically, no gross crack extension was detected in Region II, either by the conductive strips, or by observation with a traveling microscope at 20X magnification. Interior sections of samples loaded into Region II also failed to provide evidence of gross crack extension. Region III is characterized by decreases in load with increases in displacement, as is expected for a growing crack. As shown in Figure 2, measurements of crack extension derived from the conducting strips[*], show that the onset of crack extension and Region III of the load displacement curve approximately coincide. The onset of both Region II and Region III occurred at lower loads on the sandstone than in the limestone. Furthermore, and contrary to expectations, crack growth from the relatively blunt starting notches (sawcuts) proceeded in a stable rather than in an unstable fashion.

---

[*] These were confirmed by the observations with the traveling microscope.

Fracture Energy Dissipation Rates

Values of the fracture energy, R, for the limestone and the sandstone
displayed the same type of dependence on crack length, as shown in Figure 3.
From the first evidence of crack extension the R values increase up to a point
and then level out at a relatively constant value as the crack continues to
grow. This level, designated as the asymptotic limit in Table II, is the most
characteristic value of R for the rock as it defines the R associated with ex-
tension of large (relative to the grain size) preexisting flaws in the rock. A
compilation of the average R values taken from the upper plateau are given in
Table II. For the limestone, fracture on a plane parallel to the bedding plane
(AY) is accompanied by the lowest energy absorption rate while cracking on a
plane perpendicular to the bedding plane but in a direction parallel to it, (BX)
requires substantially more energy. The energy dissipation rate for the sand-
stone is larger than for the limestone and, in addition, displays a different
orientation dependence. The easy propagation plane is again the bedding plane
but the most difficult orientation is CZ, the plane and direction perpendicular
to the bedding plane. It is interesting, but probably coincidental, that the
ratios of R for the easiest and most difficult orientations are roughly the
same for both rocks. R values for comparable rocks obtained from other
sources[8,11,15] are also given in this table. While they did not report the
orientation of their crack plane their R values are comparable to the range of
data from this study.

A few tests on each rock were conducted in liquid nitrogen (-196°C).
Gilman[9] has shown that at this temperature calcite undergoes cleavage with
an R = 0.46 J/m^2, close to the specific surface energy; consequently, the
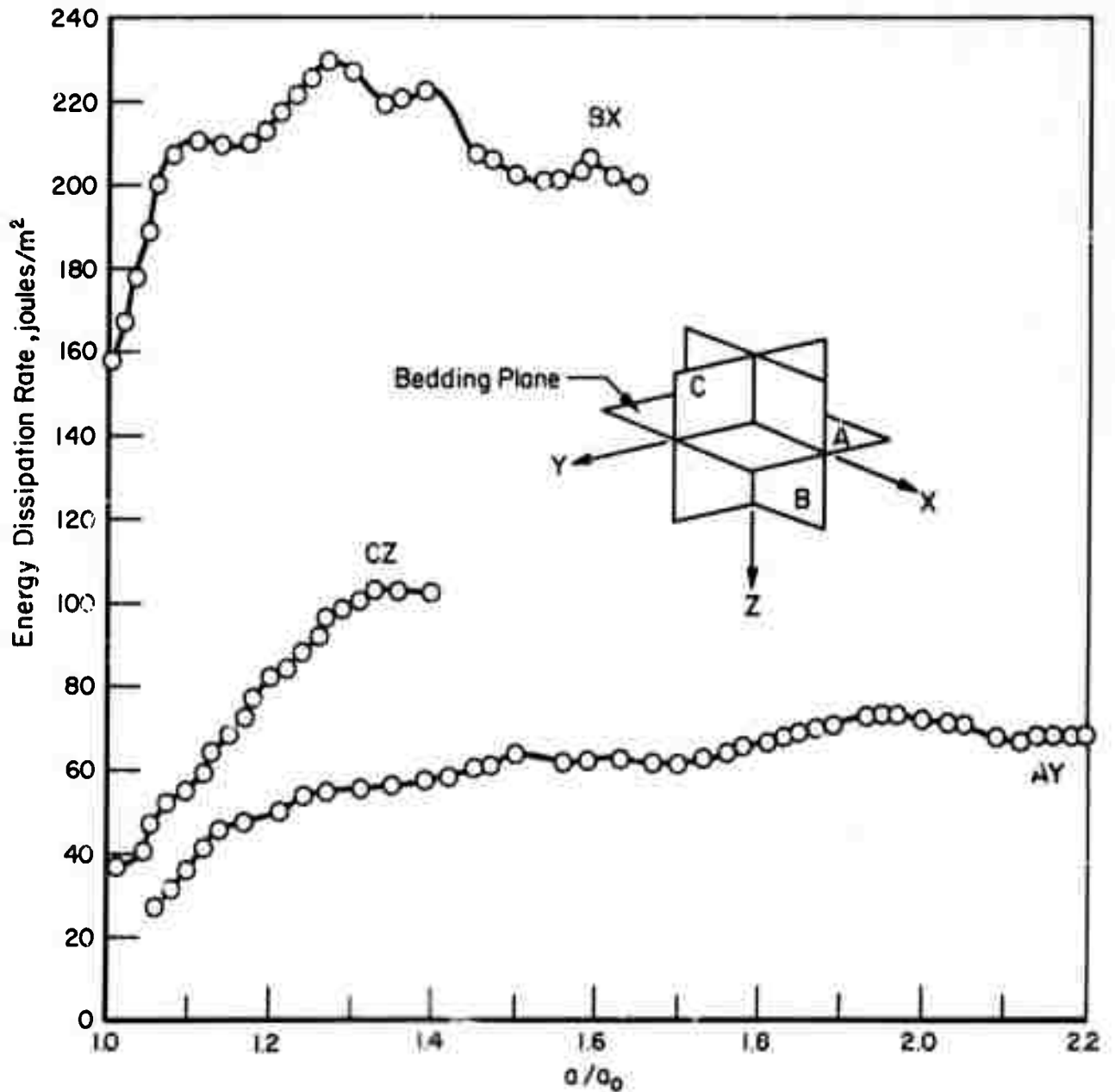energy dissipated by plastic deformation is negligible. Since the crack path

FIGURE 3. ENERGY DISSIPATION RATES MEASURED OVER AN INTERVAL OF CRACK LENGTH
FOR THREE ORIENTATIONS OF THE CRACK PLANE AND PROPAGATION DIRECTION
IN SALEM LIMESTONE. The letters A, B, and C denote orientation of
the crack plane with respect to the bedding plane (plane A) and X,
Y, and Z denote crack propagation direction. a/a_o is the ratio of
crack length to the starting slot length.

TABLE II. COMPILATION OF ENERGY DISSIPATION RATE RESULTS

Material	Orientation[a]	Asymptotic R $(joules/m^2)$
Salem Limestone		
This Study		
dry[b] (22°C)	AY	50-75
	BX	195-230
	CZ	90-110
wet[c] (-196°C)	CZ	85
	CZ	~ 40
Perkins and Bartlett[d]		84
Friedman, et al[e]		55
Berea Sandstone		
This Study		
dry[b] (22°C)	AY	465-520
	BX	600-750
	CZ	1120-1580
wet[c] (-196°C)	AY	150-270
	BX	~ 300
Perkins and Krech[f]		176
Friedman, et al[e]		139

(a) Refer to Figure 3.

(b) After baking at 110°C for 1 hour, specimens were stored in a dessicator prior to testing.

(c) Specimens were soaked in tap water for approximately 10 hours prior to testing.

(d) Reference 8. A side grooved DCB specimen was used having a width of 15.2 cm and net thickness of 3.8 cm. This R value is twice the value of surface energy quoted in References 1, 3, and 6 since $2\gamma = R$. Orientation not reported.

(e) Reference 11. A notch bend specimen was used with a thickness of 1.4 cm and beam height of 2.5 cm. Their sandstone is listed as Tennessee sandstone. These values were derived from the data of Friedman, et al, using the projected surface area. Orientation not reported.

(f) Reference 15. Same specimen design and dimensions as in Reference 1. Their sandstone is listed as Tennessee sandstone. Orientation not reported.

in both the limestone and sandstone is through calcite, a comparison of the
R value at -196°C with the room temperature value should indicate the degree
to which plastic deformation contributes to the room temperature fracture
energy dissipation processes. The results, given in Table II, show that the
R-values for limestone and sandstone are still ~ 100X to 1000X the value obtained
by Gilman. Thus, plastic deformation cannot account for the magnitude of the
R-values obtained either at room temperature or at -196°C. The authors favor
the alternative explanation that the temperature dependence of the R in the
sandstone has its origin in the difference in thermal expansion coefficients
between quartz and calcite. On cooling the sandstone to -196°C, the difference
in thermal expansion between the two components in this rock should produce
internal stresses which may, in turn, aid the applied stresses in producing
fracture. The limestone, being monomineralic, would be expected to undergo
much less, if any, differential thermal expansions leading to internal stresses.

The introduction of water appears to produce a moderate decrease
in R consistent for both rocks. The fact that the R values for both rocks
decrease by the same factor is probably related to the fact that the crack
path is through calcite in each case. Hence, environmental effects could be
expected to produce similar changes in the fracture behavior of these two
materials. There is, however, some uncertainty in the magnitude of these R
values for the wet condition because of difficulty encountered with the
conductive strips used as crack length indicators. Until a more reliable
procedure can be found for detecting the position of the crack in the wet
specimens these values should serve only as reasonable estimates.

Acoustic Emission

The tests in which acoustic emissions were monitored revealed some interesting information about the fracture mode in these materials. Examples of load-time curves superposed on an acoustic activity versus time bar graph are given in Figures 4 and 5 for the limestone and sandstone, respectively. Significant acoustic activity, which quite likely derives from cracking, is detected at loads well below the maximum load which corresponds to the point of optically observable crack extension. Furthermore, the first activity above background occurs at about the load levels at which the load-displacement record becomes nonlinear. This evidence coupled with other results described below points to the development of numerous cracks in the volume surrounding the slot tip which may, as a result, account for the gradual decrease in slope in the early stages of the test. In figure 4 the advance of the crosshead was stopped several times during this test. Upon stopping the crosshead, the acoustic activity did not terminate immediately, but instead the count rate decayed gradually, as did the load, indicating some additional growth of the crack. This behavior of crack growth under fixed displacement conditions is often observed in metals and is referred to as subcritical cracking. It is indicative of a reaction between the environment and the exposed surface at or very near the tip of the crack.

During the periods of crosshead advance the acoustic activity of the limestone was similar in level to that of the sandstone. While this may imply that the amount of cracking is the same in both rocks, it would be incorrect to conclude that this is necessarily true because differences in acoustic wave generation and transmission properties between the two rocks can markedly affect the amplitude of the signals received and, hence, the count rate.
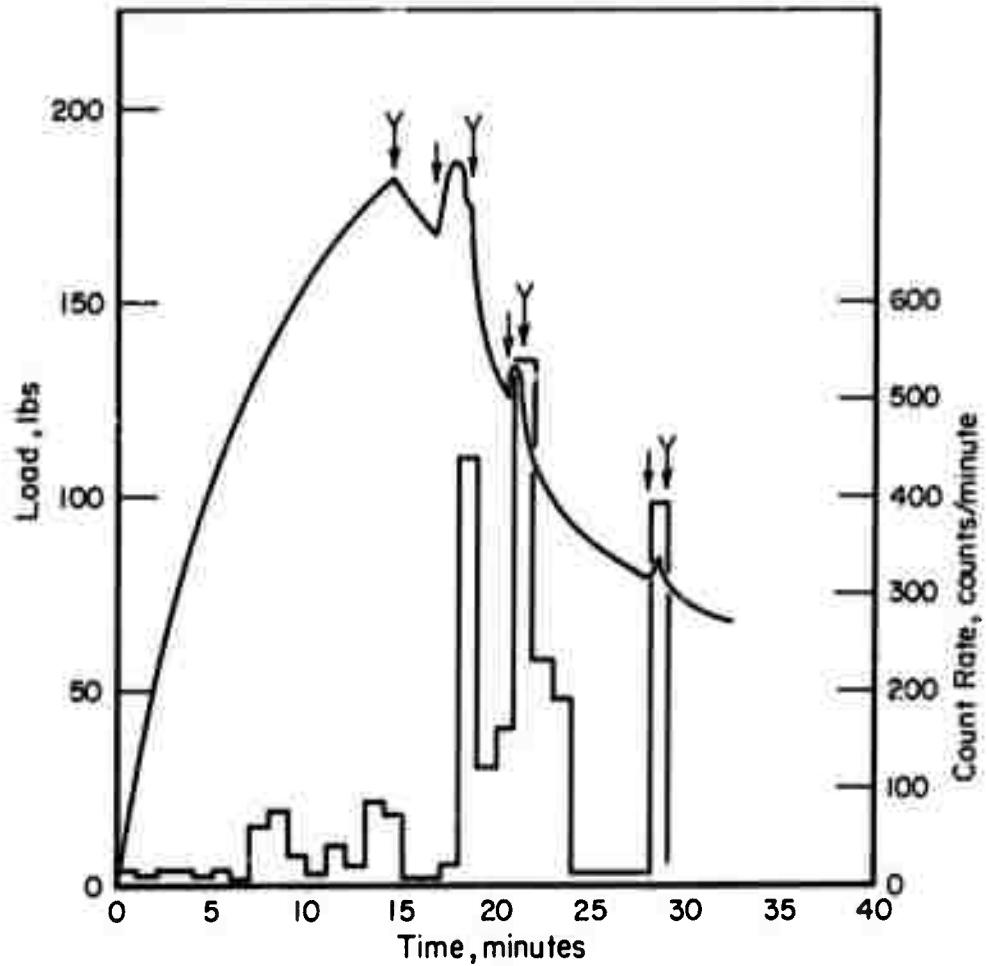
FIGURE 4. AN EXAMPLE OF THE RATE OF ACOUSTIC PULSES RECEIVED DURING TESTING OF A SALEM LIMESTONE SPECIMEN. The count rate is correlated with the wedging load applied to the specimen. The noise or background level is approximately 30 counts/minute. The crosshead advance of the testing machine was stopped at the time designated by the double-ended arrows and restarted at the single-ended arrows.
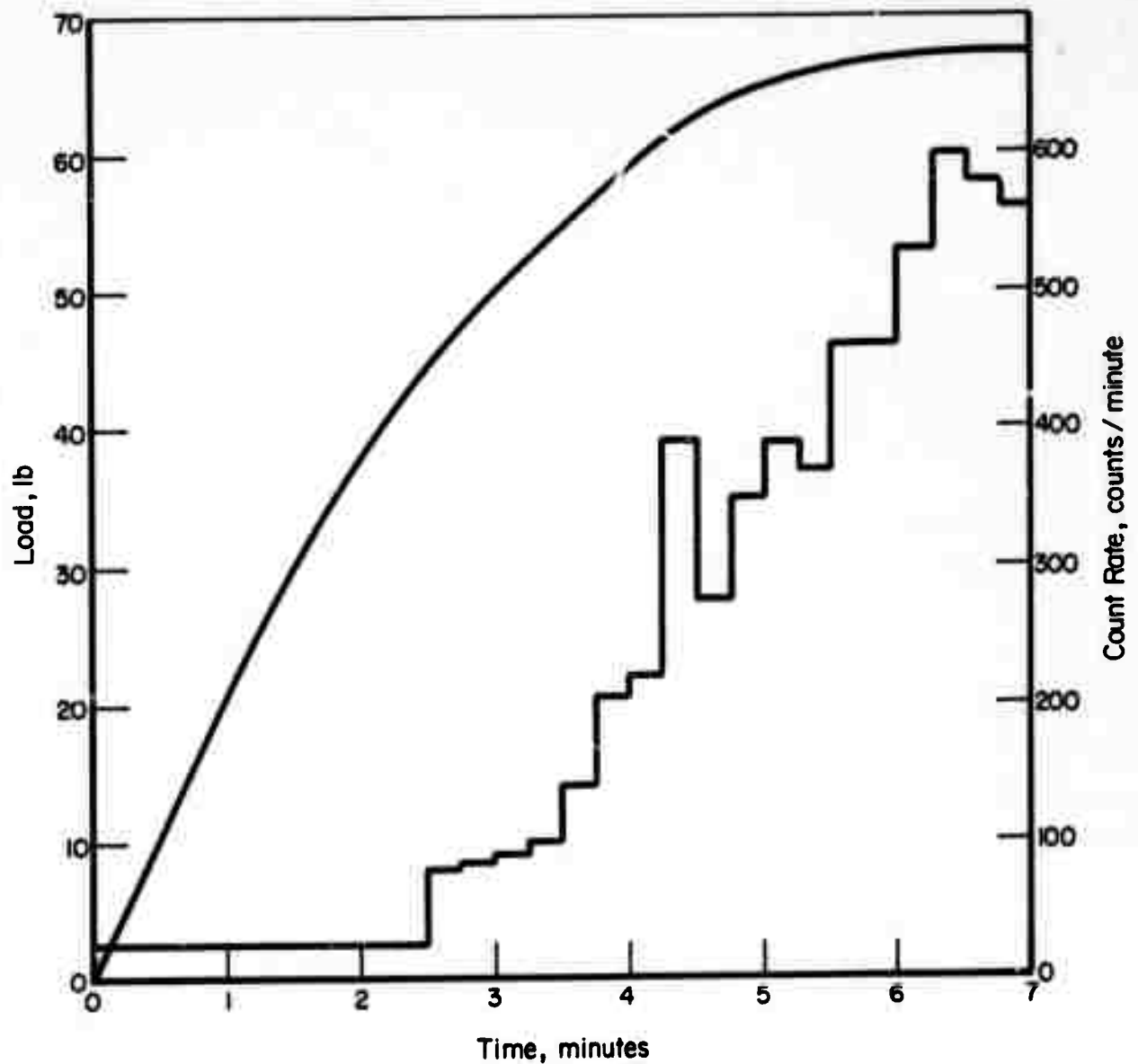
FIGURE 5. AN EXAMPLE OF THE RATE OF ACOUSTIC PULSES RECEIVED DURING TESTING OF A BEREA SANDSTONE SPECIMEN. Here the background level is about 25 counts/minute and the crosshead was not stopped during the test.

Microscopic Studies of the Salem Limestone

The microstructure of the Salem limestone specimens consists of an
aggregate of particles identifiable as calciferous fossils or fragments of
fossils together with öolites. The particles are loosely packed and consider-
able pore space is observable. The diameters of the particles in this aggregate
are principally in the range of 0.5 mm to 2.0 mm. At low magnification (~ 30X)
the particles appear to be cemented by a white powdery material (the matrix).
At higher magnifications the granular character of the matrix is observable as
can be seen in Figure 6 which shows electron micrographs of a replica made from
a polished and lightly etched surface. Both views in Figure 6 show the structure
within the matrix or at the interface of a larger particle (öolite or fossil
fragment). The fine particles comprising the matrix appear to have a diameter
of about 1 μ. The reflecting optical micrographs in Figure 7 display the
heterogeneous nature of the microstructure and also show the path of the crack.
The micrographs in Figure 7 were obtained from a polished surface of a specimen
with a crack of the AY orientation. The specimen was first prepared for obser-
vation by infiltrating the crack and the interconnecting pores with an epoxy
in order to prevent tearing out of loose material during polishing. These
micrographs indicate that the crack propagates most often through the matrix
described above. There is, however, considerable fracture of the fossil debris
and öolites as can be seen in Figure 7. Note also that because the crack pre-
dominantly follows the matrix, the path is highly irregular and, therefore, the
actual surface area created during fracturing is larger than the area referred
to in Equation (2) and on which the calculation of R is based.
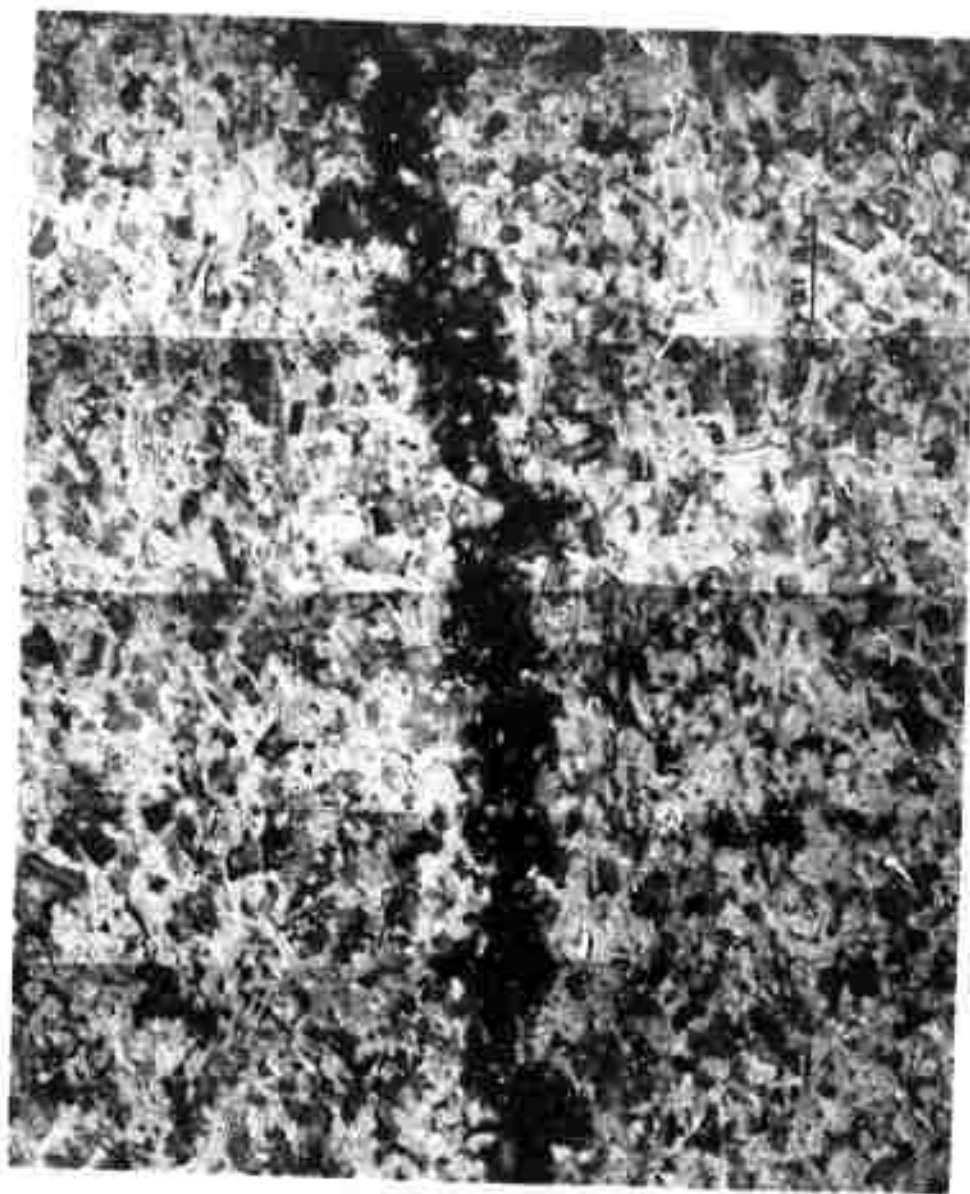
(b)

(a)
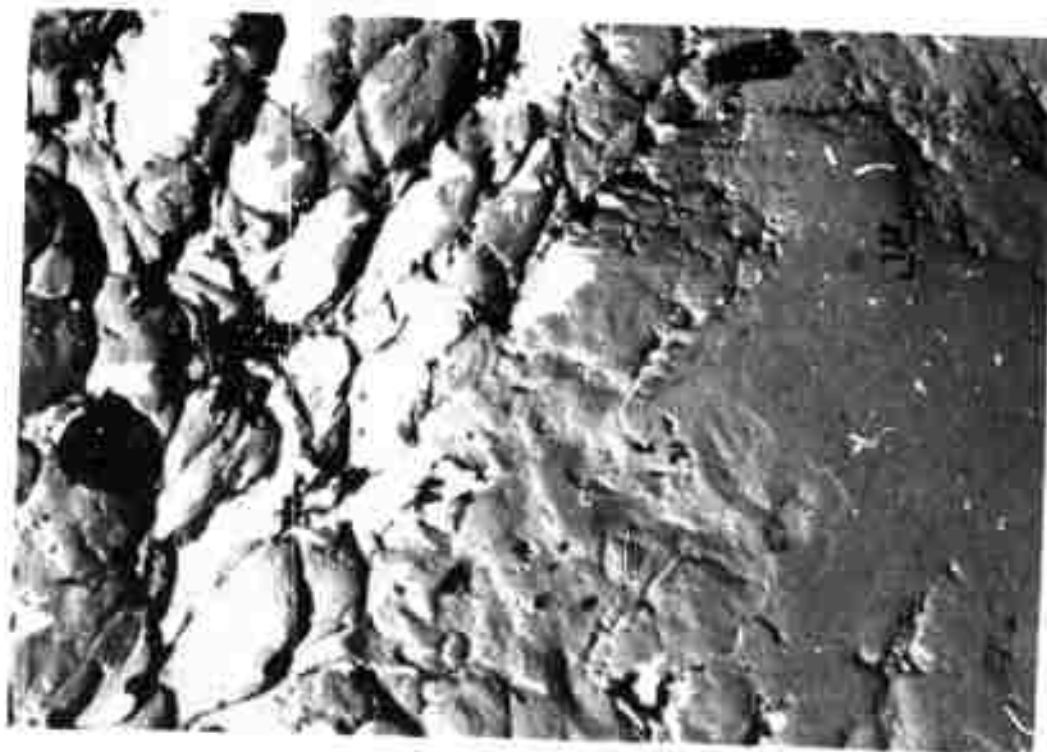
FIGURE 6. EXAMPLES OF MICROSTRUCTURE REVEALED BY ELECTRON MICROSCOPY OF REPLICAS OF A POLISHED AND ETCHED SURFACE OF INDIANA LIMESTONE (etchant: 50% HF, 50% glacial acetic).

FIGURE 7. CRACK PROFILES AT THE MIDTHICKNESS PLANE OF A SALEM LIMESTONE SPECIMEN. The specimen has been impregnated with an epoxy resin: (a) region near the initial slot tip and (b) region containing the crack tip.

(a)
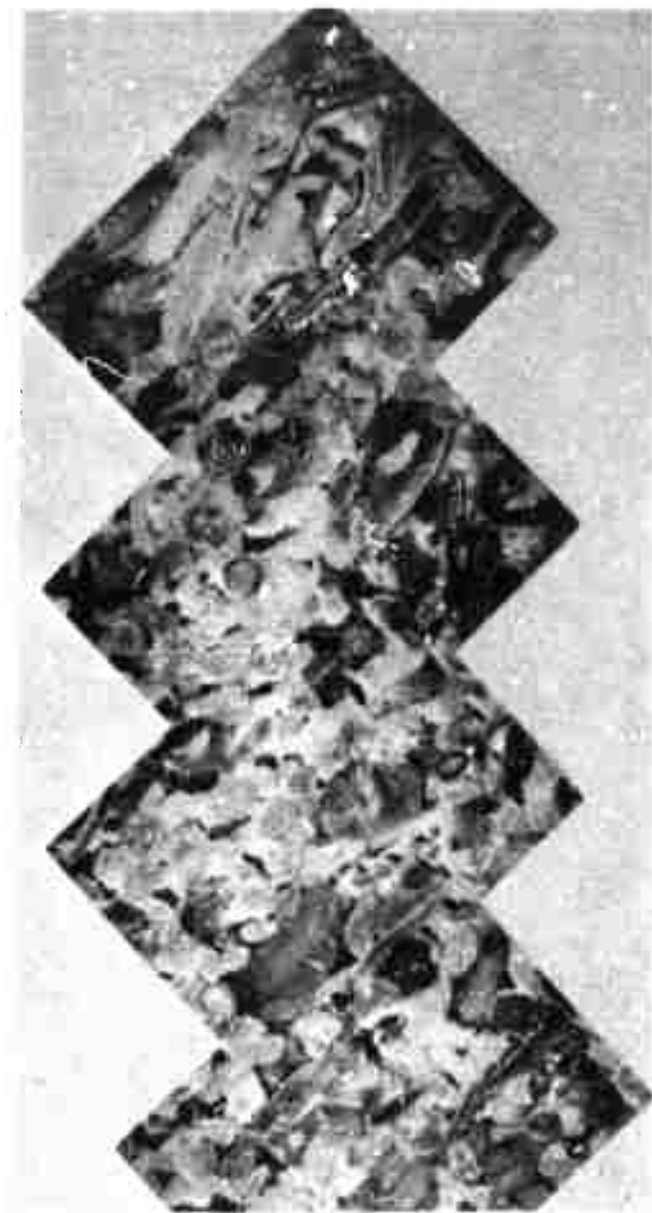
(b)

FIGURE 7. CRACK PROFILES AT THE MIDTHICKNESS PLANE OF A SALEM LIMESTONE
SPECIMEN (Continued).

Proceeding to higher magnifications of the fracture surface reveals more clearly the highly irregular character of the surface topography. Figures 8a, b, and c are a sequence of stereo pairs[*] of progressively increasing magnification made by scanning electron microscopy of an area of the fracture surface of a Salem limestone specimen. In Figure 8a, the outline of a number of millimeter size particles are observable. Figure 8b reveals an area where the crack has passed partially through the matrix material as well as through larger particles. The fracture surfaces of the larger particles (whether fossil fragments, precipitated crystals, or öolites) display distinct patterns. reminiscent of cleavage of single crystals. Verification that these are single crystals of calcite or at least highly oriented polycrystals is discussed in reference to Figure 9. At high magnification the fine micron size particles comprising the matrix appear to be faceted as shown in Figure 8c which suggests that these also may be single crystals. The utility of the scanning electron microscope derives from the large depth of focus it provides at all levels of magnification. A good example of this capability is shown in Figure 8d which reveals a pore broken open during fracture and which contains a lining of nearly perfect crystals of calcite or perhaps magnesite.
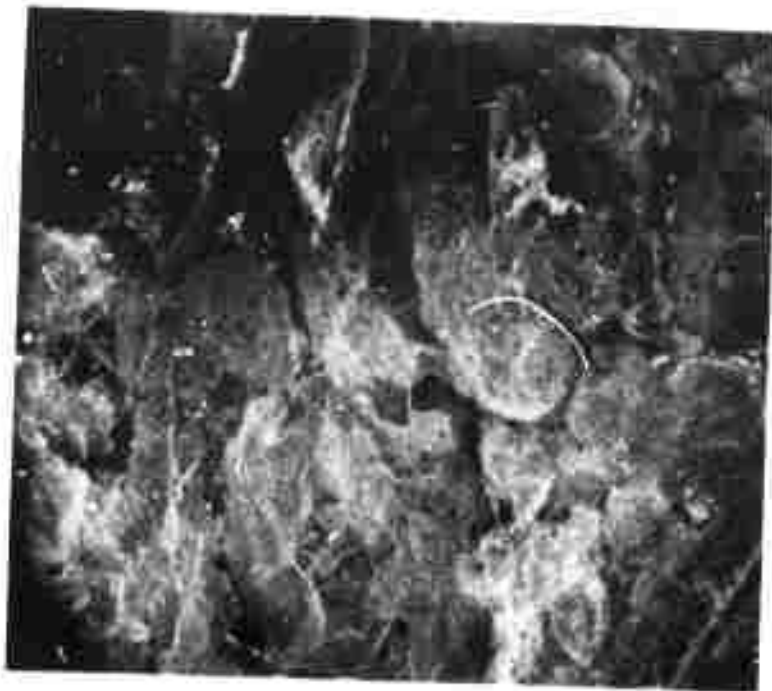
In order to resolve features as small as 20 angstroms, plastic replicas were made of the fracture surfaces. A platinum-carbon mixture was then vapor deposited onto the plastic replica which, in turn, was then dissolved in acetone. The Pt-C films are placed in an electron microscope in which an electron beam passes through the films and the resulting image can be displayed on a phosphor screen or photographed. During the replication process

---

[*] A three-dimensional effect is obtained when viewing these micrograph pairs through a stereo viewer. If such a veiwer is available the pages should be removed and slit down the center in order to adjust the spacing between the micrographs for the viewer used.
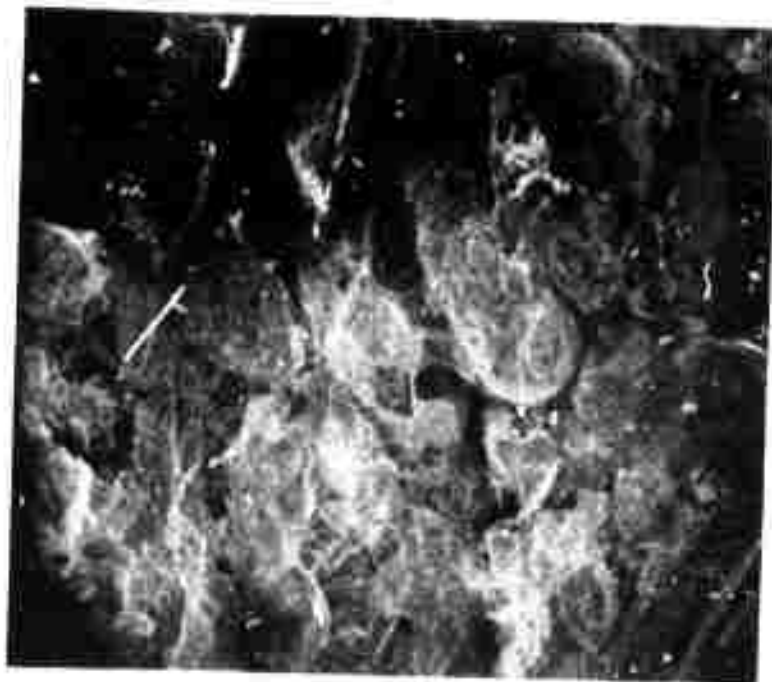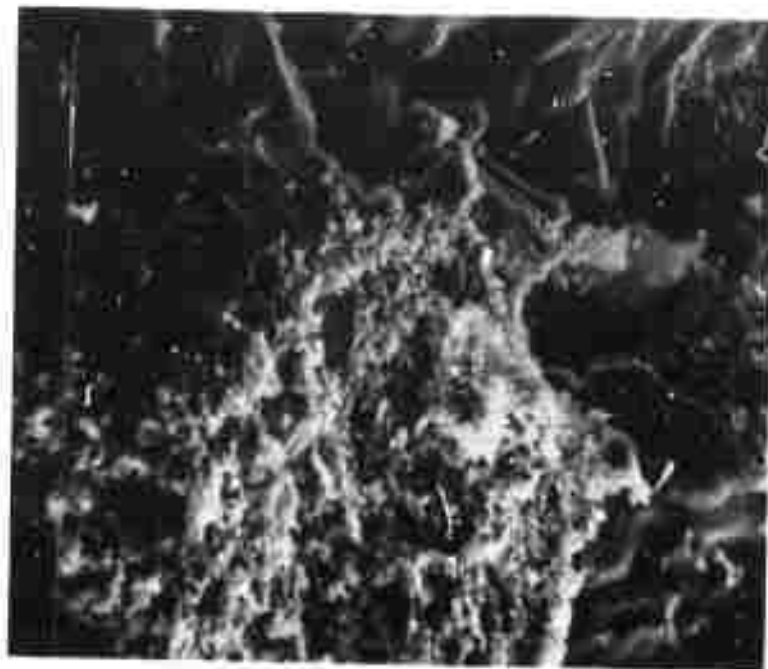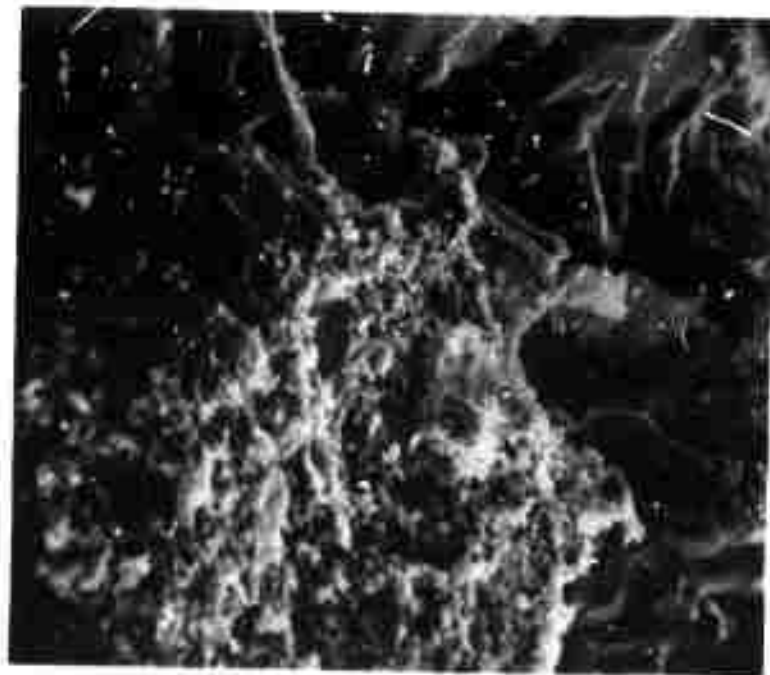
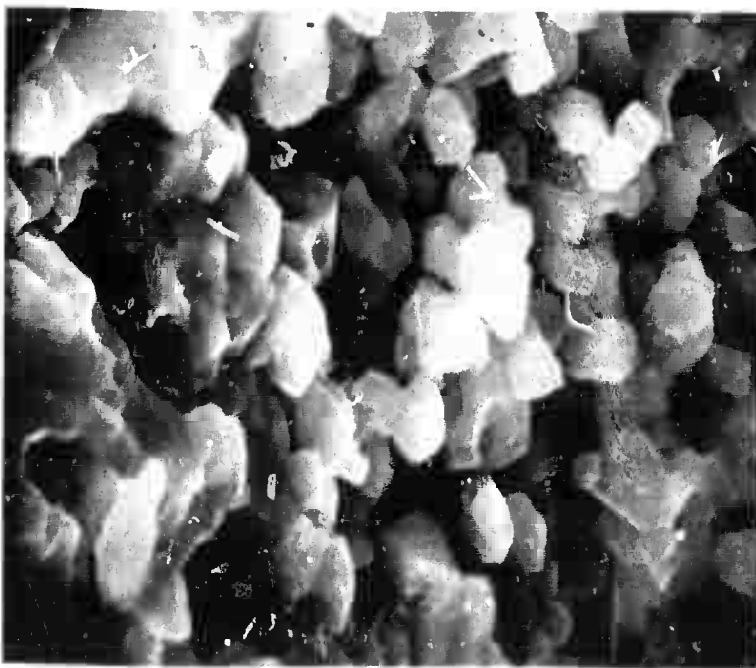(a) Low magnification view of fracture surface revealing outlines of broken fossils and oolites. (50X)

FIGURE 8. STEREO PAIRS OBTAINED BY SCANNING ELECTRON MICROSCOPY OF FRACTURE SURFACE IN SALEM LIMESTONE.

23

(b) Here the crack has passed partially through the crystalline öolites as well as through the much finer aggregate of particles cemented between the öolites. (500X)

FIGURE 8. STEREO PAIRS OBTAINED BY SCANNING ELECTRON MICROSCOPY OF FRACTURE SURFACE IN SALEM LIMESTONE (Continued).
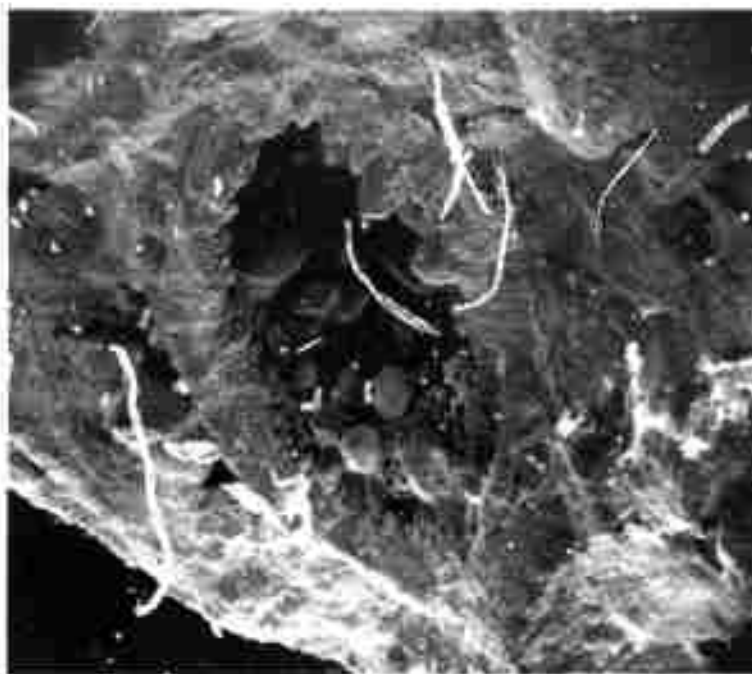
2.4

(c) More detail of the fine interöolite aggregate on the fracture surface. (5000X)

FIGURE 8. STEREO PAIRS OBTAINED BY SCANNING ELECTRON MICROSCOPY OF FRACTURE SURFACE IN SALEM LIMESTONE (Continued).

(d) Apparently nearly perfect calcite crystals precipitated within a small cavity which has been broken open during fracturing. (50X)

FIGURE 8. STEREO FAIRS OBTAINED BY SCANNING ELECTRON MICROSCOPY OF FRACTURE SURFACE IN SALEM LIMESTONE (Continued).

of the limestone, small fragments on the fracture surface were removed and could be observed in the final replica. For example, Figures 9a and 9b show the outlines of numeorus micron size particles comprising the matrix, as well as the impression in the replica of areas of the surface. Contrast the irregular character of this surface with the relatively flat cleavage surface of one of the millimeter size particles in Figure 9c. The distinct feature in Figure 9c is known as a river pattern and occurs when the crack passes from one single crystal into another with a very slight difference in crystallographic orientation. It was also discovered that thin flakes of material were removed from these cleavage surfaces. These flakes were thin enough to be transparent to the electron beam thereby relevating the internal structure as can be seen, for example, at ultra-high magnification (108,000X) in Figure 9d. In addition, electron diffraction patterns can be obtained from these flakes, an example of which is shown in Figure 9e. These patterns can be used to make relatively precise determinations of crystal structure. The pattern in Figure 9e has been analyzed and was found to correspond with the structure of single crystal calcite.

Microscopic Studies of the Berea Sandstone

The microstructure consists of remarkably uniform-sized quartz grains (0.3 mm dia.), cemented by calcite. A considerable number of voids are evident and Handin, et al[16] report a volume fraction of pores of 18%. The main crack propagates through the interconnecting calcite layers. Figure 10 provides some evidence that prior to and accompanying the propagation of the main crack there is extensive cracking occurring in a relatively large volume of material adjacent to the crack. During vacuum impregnation of the sandstone, with epoxy resin, penetration was typically only 2 to 3 mm into the surface. However,
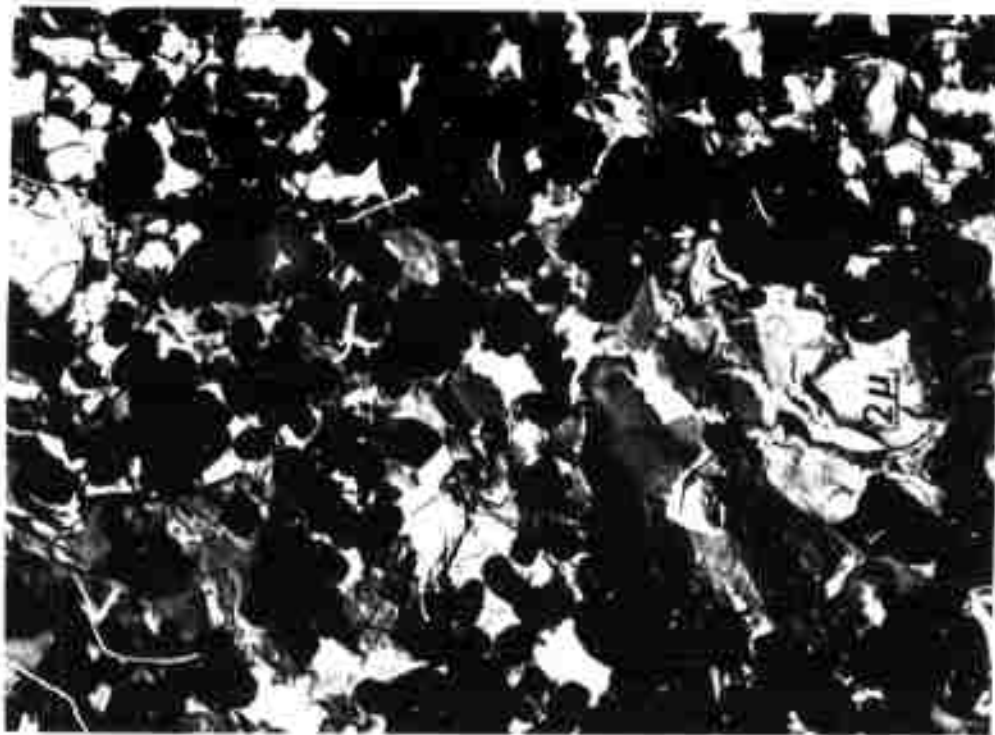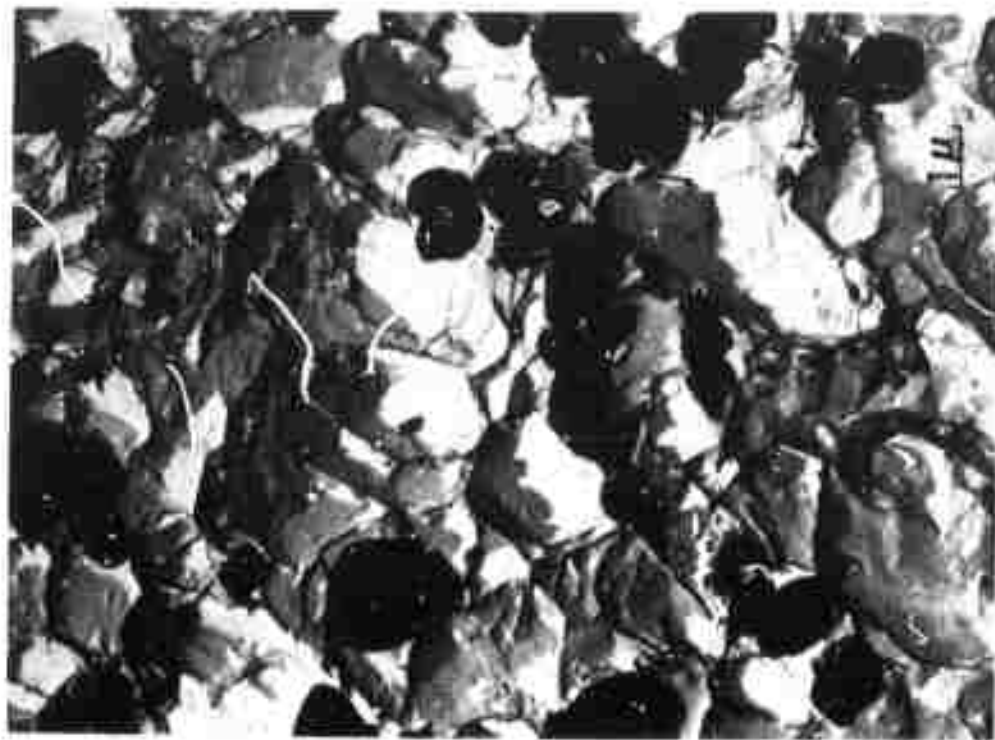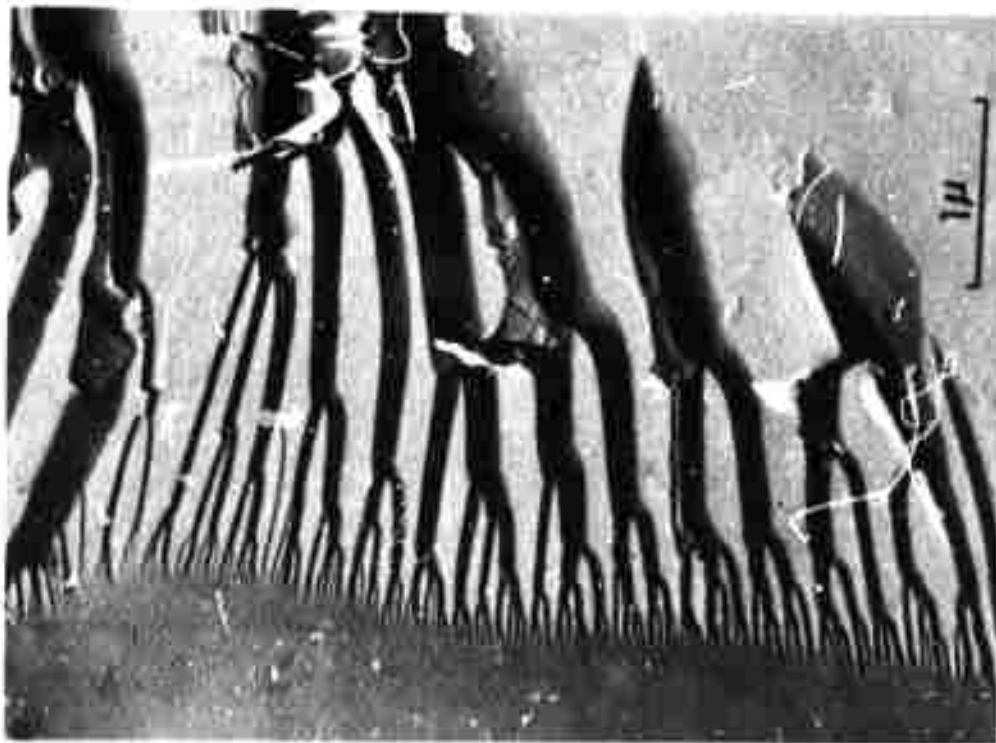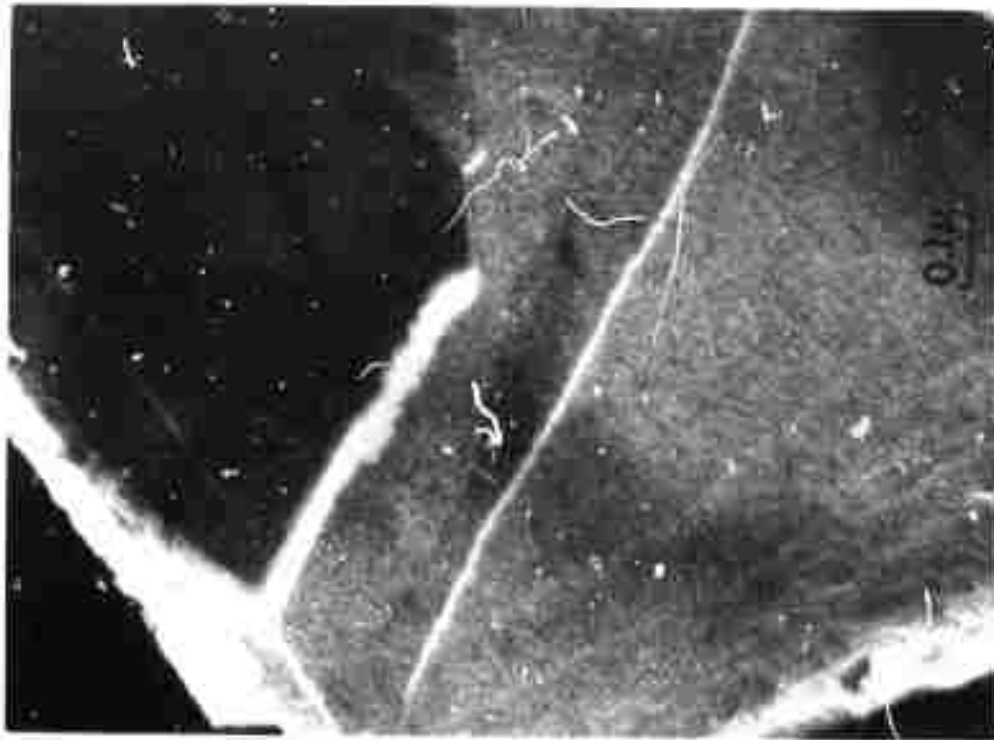
(b)

Micron size interoölite particles extracted from the fracture surface.

(a)

FIGURE 9. HIGH RESOLUTION ELECTRON MICROSCOPE FRACTOGRAPHS OBTAINED FROM Pt-C SHADOWED REPLICAS OF THE FRACTURE SURFACE OF SALEM LIMESTONE.

(d) A thin flake extracted from a cleavage surface (note that the flake is thin enough to be partially transparent to the beam thereby revealing some internal structure).

(c) An example of cleavage

FIGURE 9. HIGH RESOLUTION ELECTRON MICROSCOPE FRACTOGRAPHS OBTAINED FROM Pt-C SHADOWED REPLICAS OF THE FRACTURE SURFACE OF SALEM LIMESTONE (Continued).

(e) A thin flake extracted from a cleavage surface and the associated electron diffraction pattern.

FIGURE 9. HIGH RESOLUTION ELECTRON MICROSCOPE FRACTOGRAPHS OBTAINED FROM Pt-C SHADOWED REPLICAS OF THE FRACTURE SURFACE OF SALEM LIMESTONE (Continued).

FIGURE 10. CRACK PROFILES AT THE MIDTHICKNESS PLANE OF A BEREA SANDSTONE SPECIMEN. The specimen has been impregnated with an epoxy resin. Note the elliptical zone of penetration of the resin surrounding the slot tip.

around the tip shown in Figure 9 the material is much more permeable as can be seen by the boundary of the epoxy extending farther than 1 cm from the slot tip. Furthermore, during sectioning of specimens containing a crack, it was noticed that quartz grains adjacent to the crack were quite loose and could be easily removed.

On the fracture surface at relatively low magnifications, individual quartz grains are readily observable as can be seen on the stereo pairs obtained by scanning electron microscopy in Figure 11. The grains, exhibit both irregular surfaces and planar facets. There is also some indication here of very narrow cracks in the seams between individual grains. In fact, at 100X (Figure 11a) the SEM fractographs give an appearance of loosely adherent rubble. This appearance is somewhat consistent with the fact that after the sandstone specimens were completely broken open a large number of particles would fall from the fracture surfaces and many more could be dislodged with a slight tap. Figure 11 b shows the only evidence of cracking of the quartz grains that was found. This shows an area of conchoidal fracture with a small chip partially broken away from the underlying quartz grain. In Figure 11c the calcite cement can be identified as the aggregate of small rather blocky particles. Another area of calcite is shown at higher magnification (2000X) in Figure 11d. The calcite appears as a well-defined polycrystalline aggregate displaying many surfaces identifiable as cleavage surfaces. These cleavage surfaces are distinguished by a river pattern on the surface, an excellent example of which is shown in Figure 12a which is obtained by electron microscopy of a replica from the fracture surface. It cannot be firmly established whether cleavage areas in Figure 12a are in the quartz or the calcite but their general appearance is similar to the cleavage morphology found in the limestone, and it is likely that
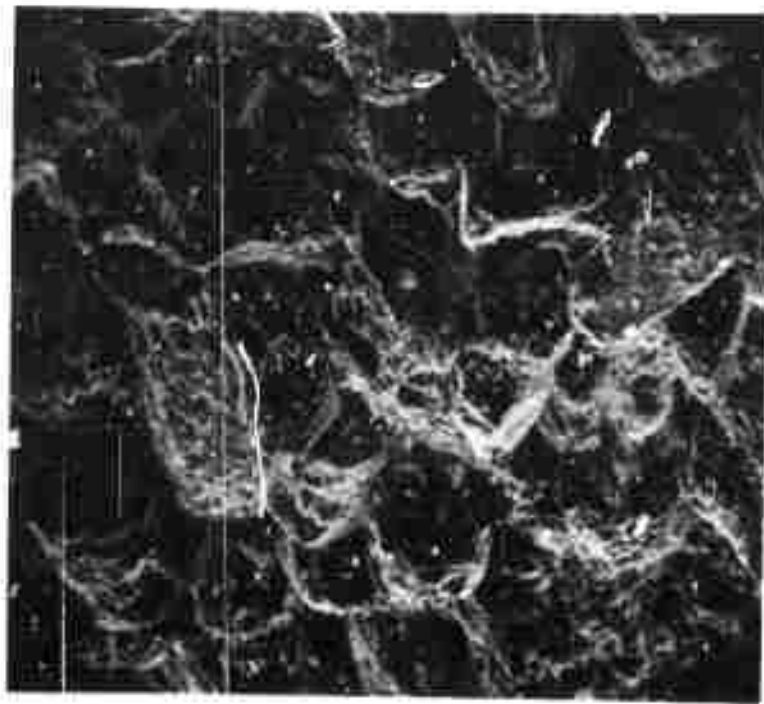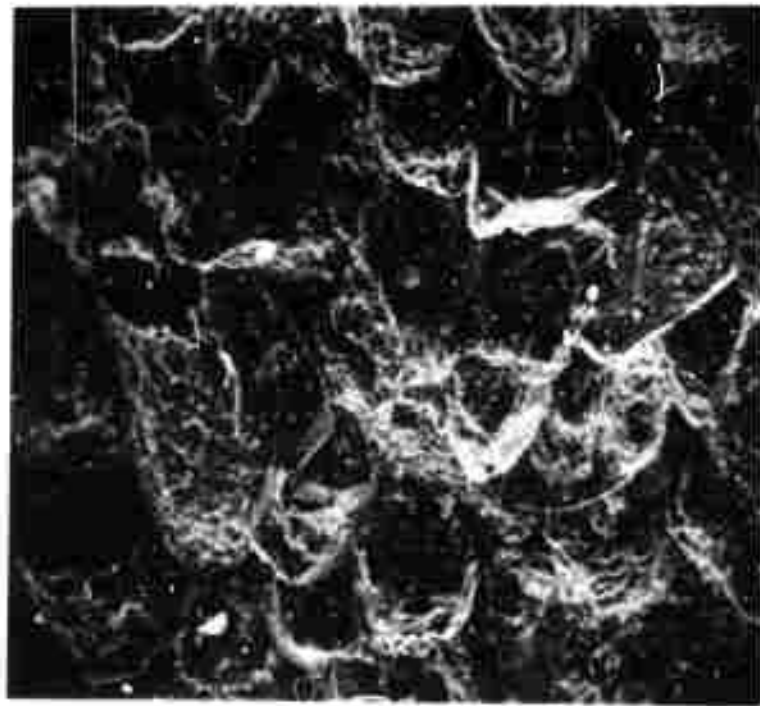
(a) The surface at 100X revealing the quartz grains and the finely divided calcite on the surface of the grains. Note the cracks which disappear under the grains.

FIGURE 11. STEREO PAIRS OBTAINED BY SCANNING ELECTRON MICROSCOPY OF THE FRACTURE SURFACE OF BEREA SANDSTONE.
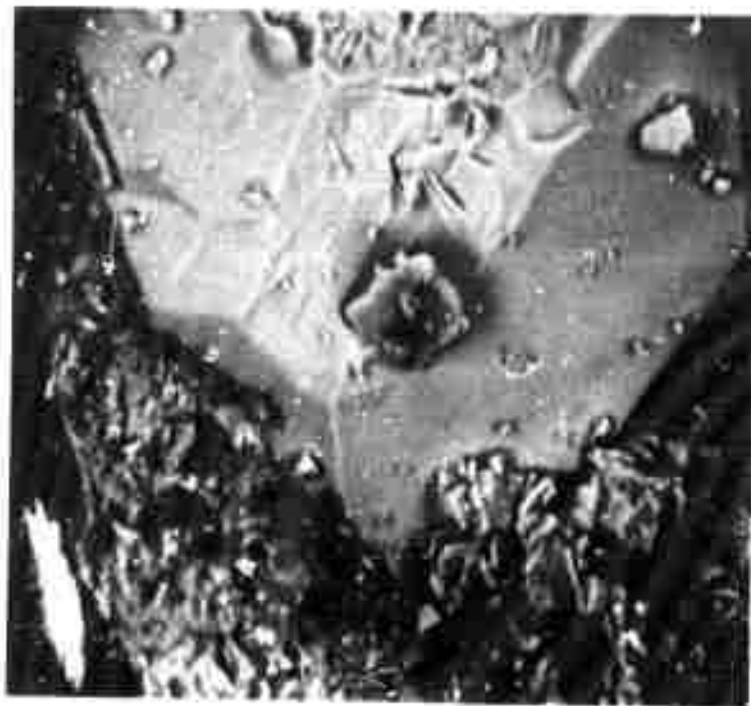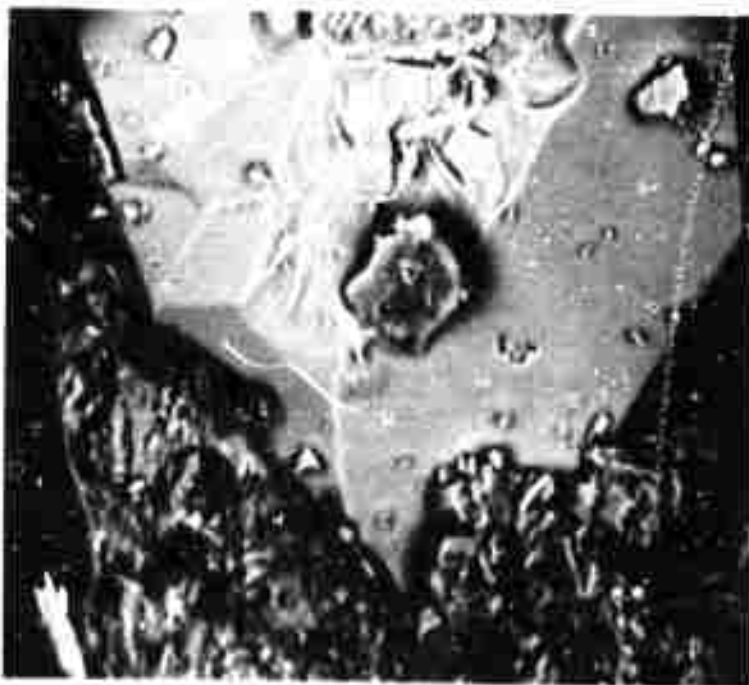
(b) A partially chipped quartz grain. This view coincides with an area slightly to the right of center in (a). 500X

FIGURE 11. (Continued)

34
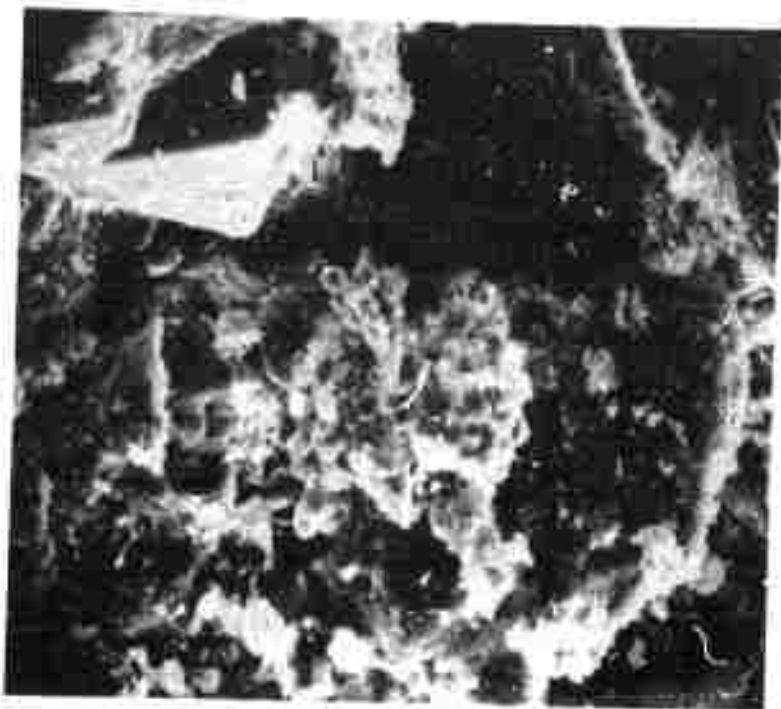
(c) A small aggregate of calcite is located at the center of the field. 500X

FIGURE 11. (Continued)
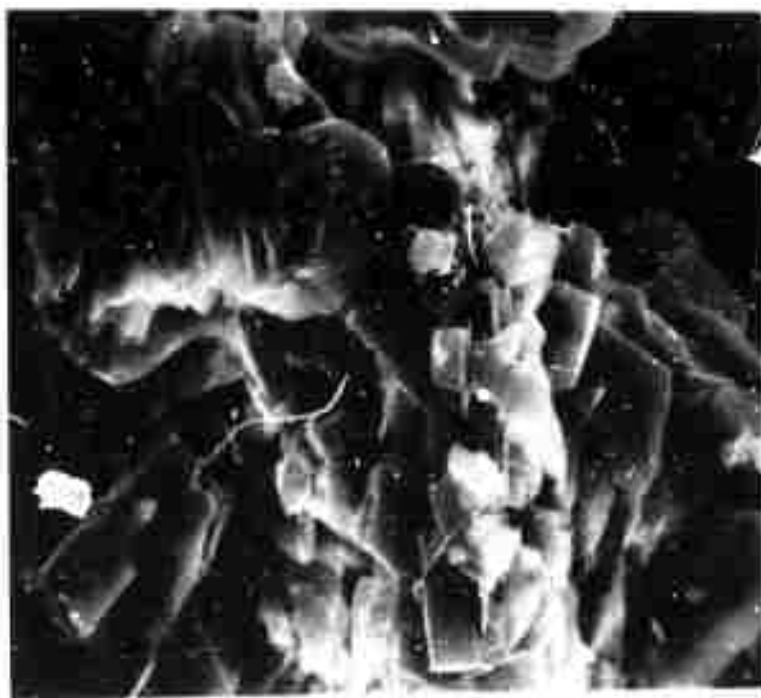
(d) A calcite aggregate at 2000X.

FIGURE 11. (Continued)
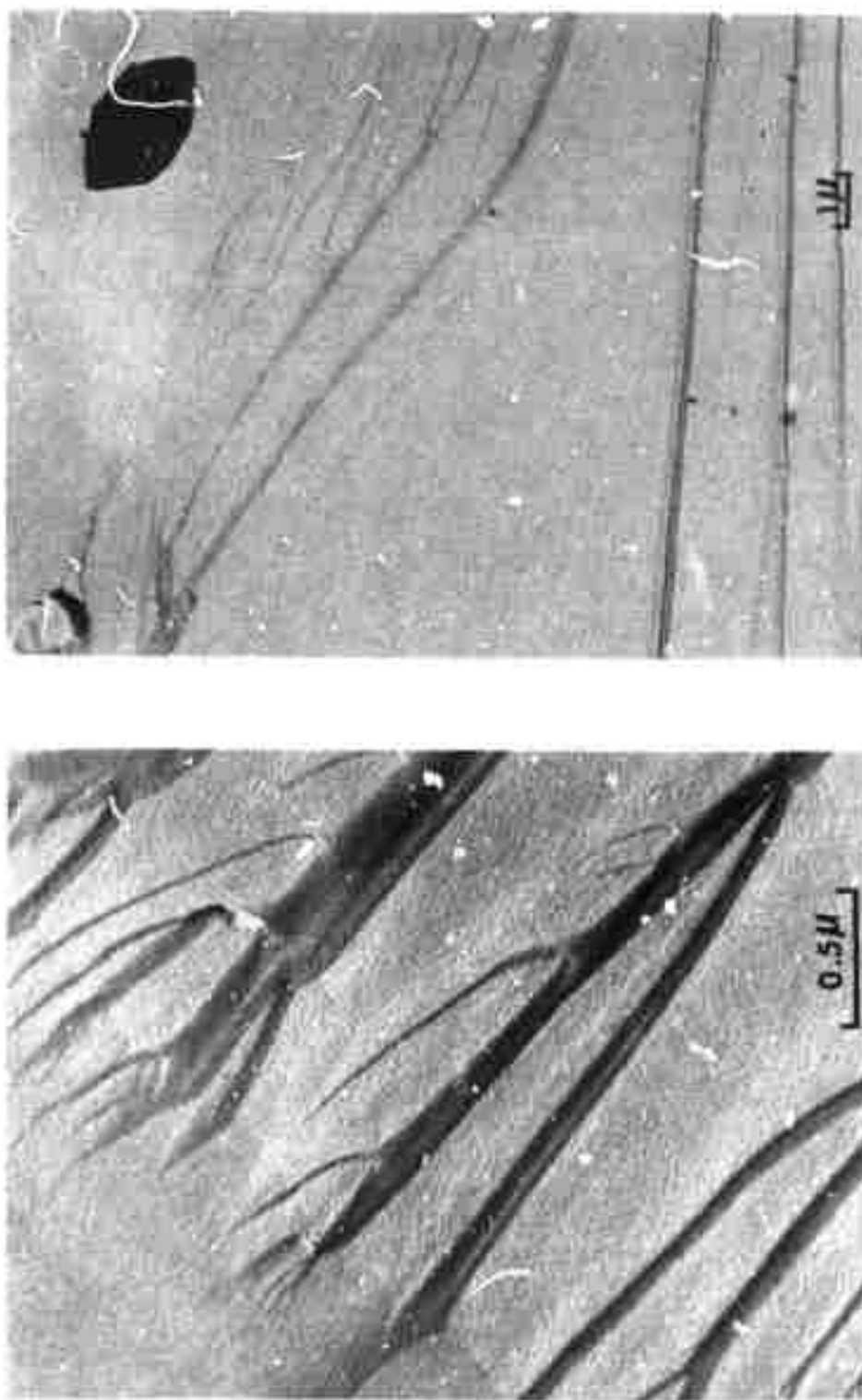
(a)

FIGURE 12. HIGH RESOLUTION ELECTRON MICROSCOPE FRACTOGRAPHS OBTAINED FROM Pt-C SHADOWED REPLICAS OF THE FRACTURE SURFACE OF BEREA SANDSTONE: (a) areas of distinct cleavage and (b) secondary silica deposits.

0.5μ

37

these cleavage areas, which were common on the replicas, predominantly represent
the fracture surface of the calcite cement. The other feature commonly observed
is shown in Figure 12b and probably is representative of the surface of quartz
grains. These blocky crystals exhibit typical habit planes of quartz and are
similar to features found on the surface of quartz grains by Kirkpatrick and
Summerson[17]. Therefore, these surfaces probably form the pore walls and are
not produced as the result of fracture.

When examining the stereo pairs one obtains a very vivid portrayal
of highly uneven relief of the fracture surface in these materials. Some quanti-
tative measurements of this relief were made from Figures 11a, c, and d by means
of a Hilger and Watts stereoscope. The resulting elevation profiles are shown
in Figures 13a, b, and c along with an inset which indicates the position of the
profile on each of the SEM fractographs. At 100X, Figure 13a, the profiles of
individual quartz grains are easily recognized and going to 500X offers little
additional information concerning the topography. However, at 2000X in Figure
13c, the faceted character of the calcite cement becomes obvious, a feature
which cannot be distinguished in the profiles at lower magnification.

The great usefulness of these elevation profiles is that they provide
a means for estimating the exposed surface area by simply squaring the actual
length of the line representing the profile. The overall profile length can
be most adequately obtained from the magnifications at 10X, 100X, and 2000X.
The profile length is longer than the horizontal distance by a factor of approxi-
mately 1.2, 1.6, and 1.7 at each of these magnifications, respectively. There-
fore, the total profile length determinable up to a magnification of 2000X is
simply the product of these factors or about 3.3 times the horizontal distance.
This gives an exposed surface area which is about 11 times the projected surface
area.
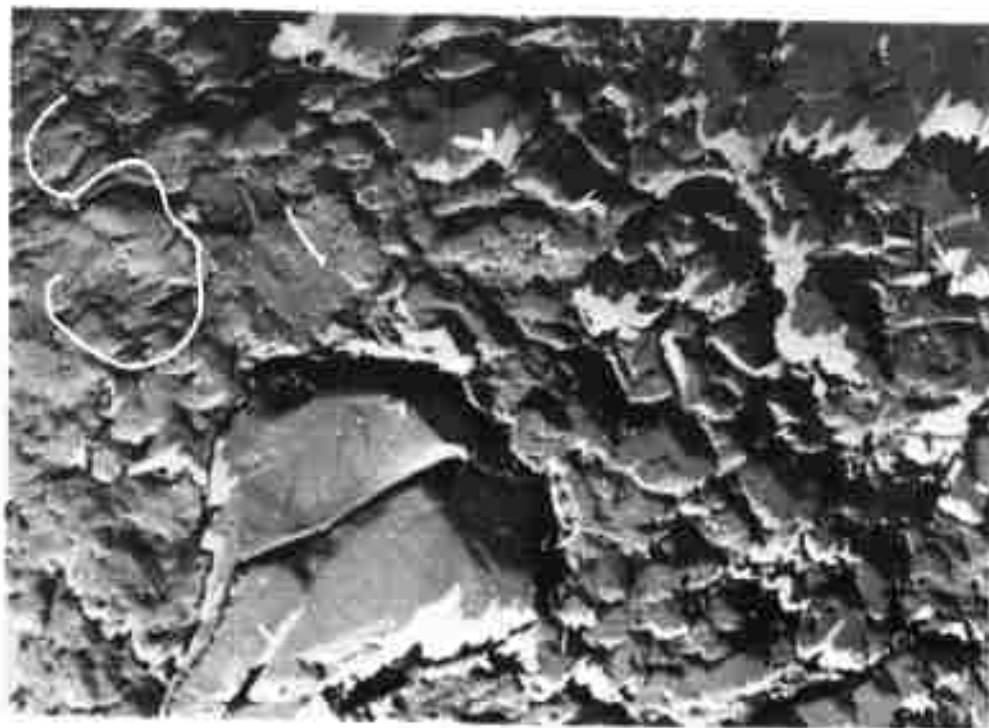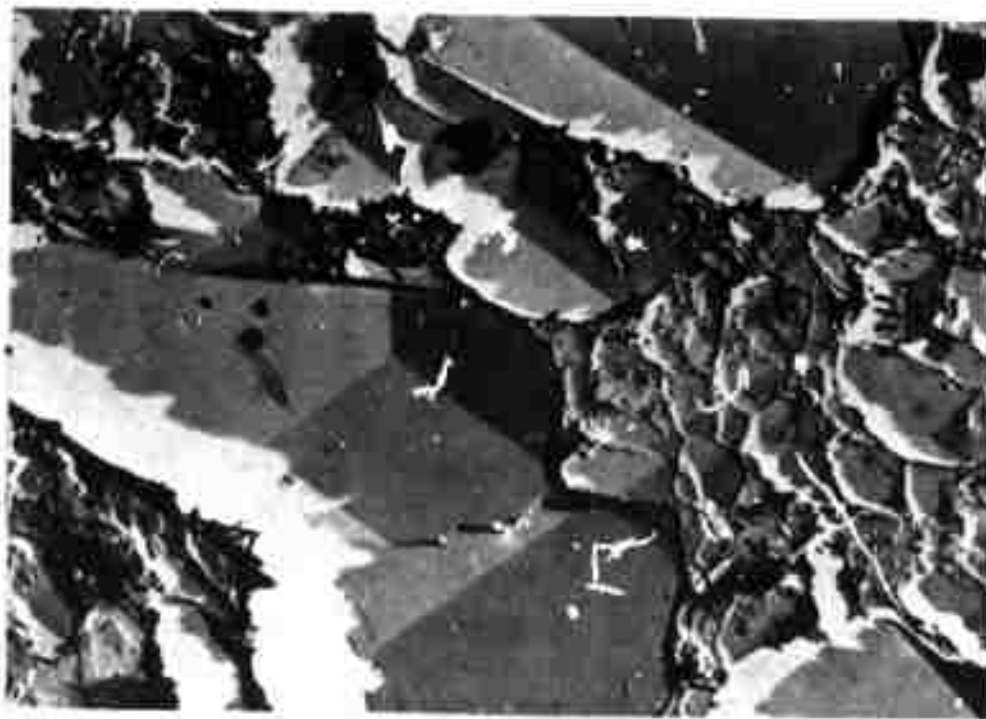
(b)

FIGURE 12. HIGH RESOLUTION ELECTRON MICROSCOPE FRACTOGRAPHS OBTAINED FROM Pt-C SHADOWED REPLICAS OF THE FRACTURE SURFACE OF BEREA SANDSTONE (Continued).
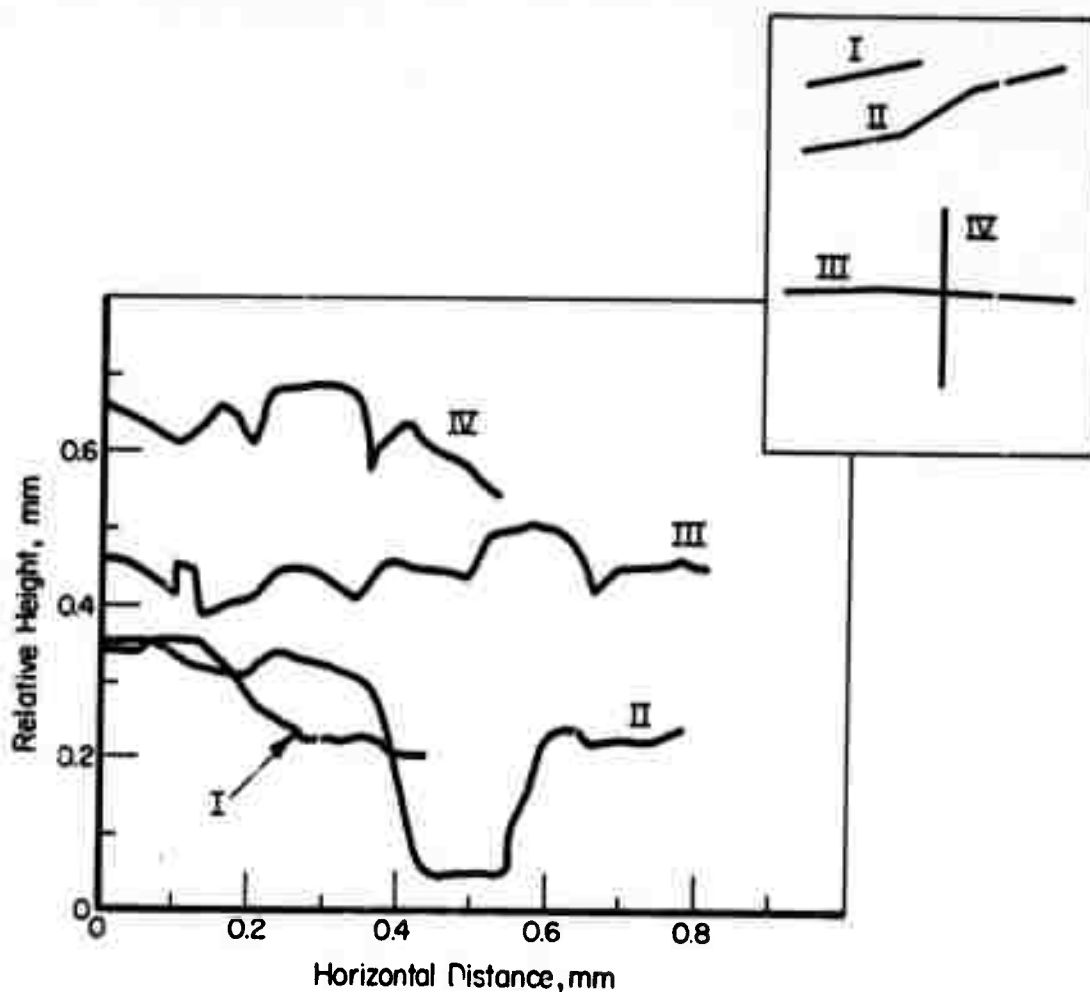
(a)

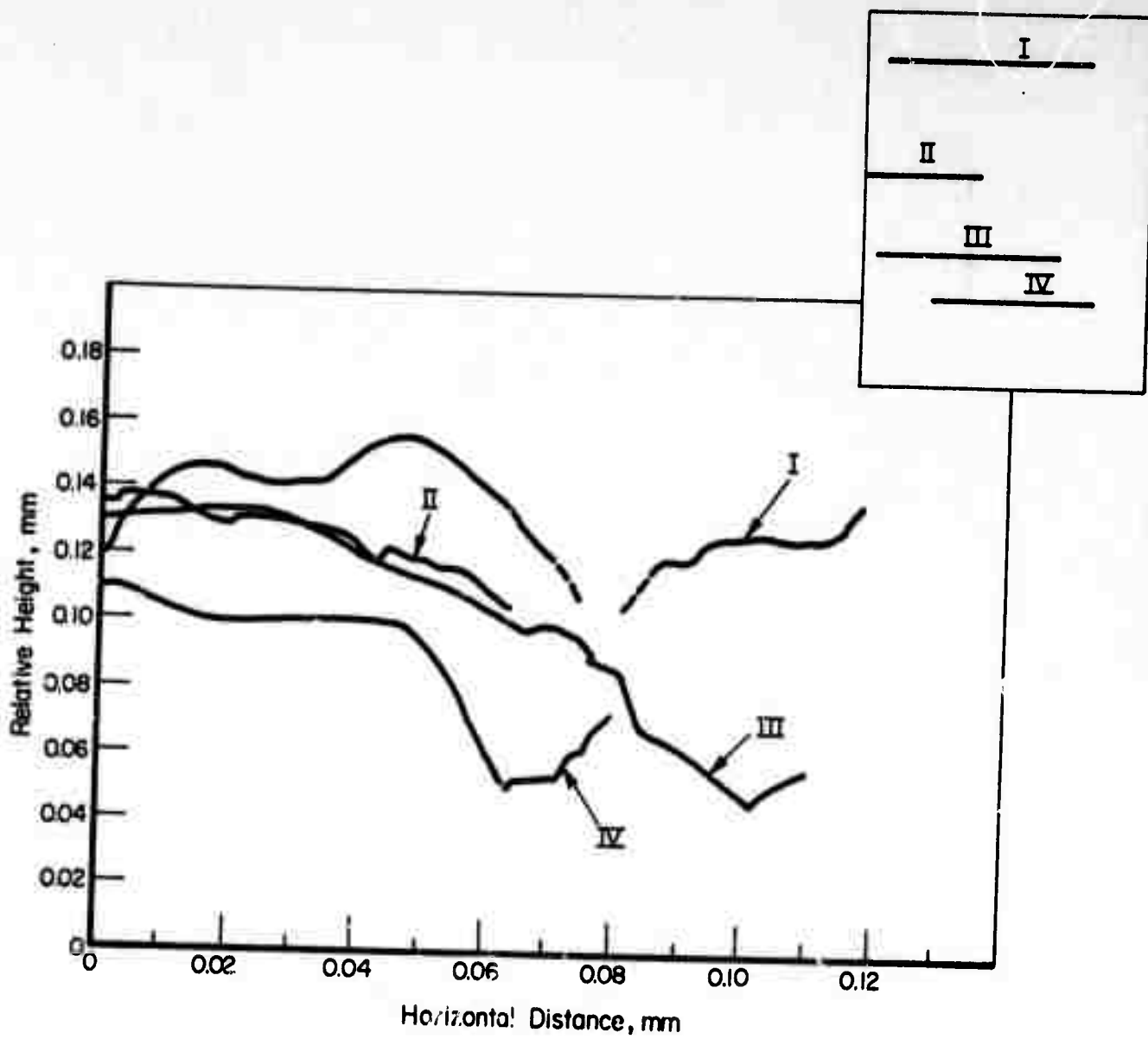FIGURE 13. ELEVATION PROFILES OF THE FRACTURE SURFACE OF BEREA SANDSTONE. These profiles were measured using a Hilger and Watts stereoscope from the stereo pairs in Figure 11. The inset shows the location of each profile on the corresponding figure.

      (a) From Figure 11a at 100X.

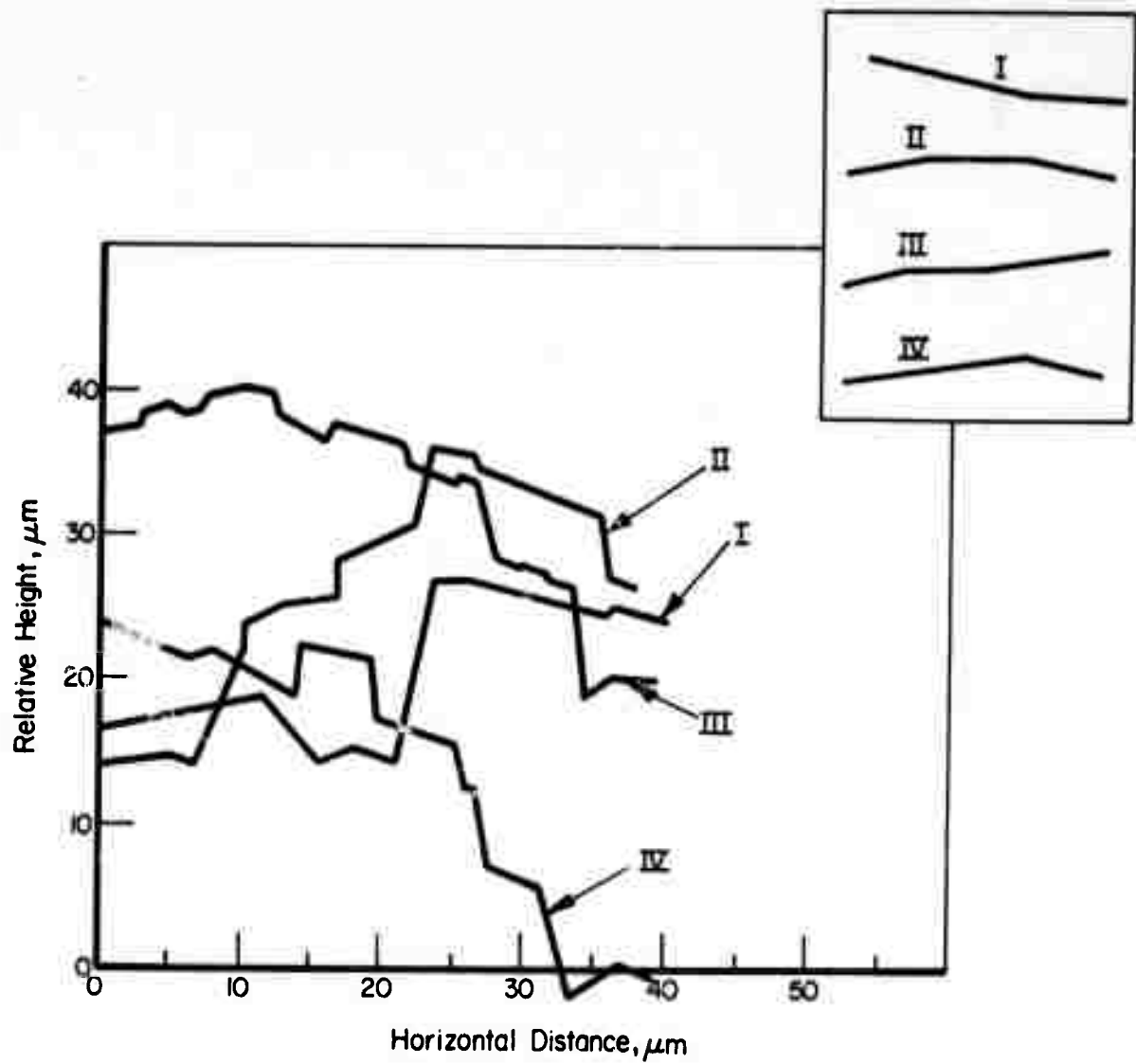   (b) From Figure 11c at 500X.

      (c) From Figure 11d at 2000X.

(b)

FIGURE 13. (Continued)

(c)

FIGURE 13. (Continued)

DISCUSSION

The results obtained in this study favor the interpretation of Moavenzadeh and Kuguel[10] and Friedman and coworkers[11], which ascribes the relatively large fracture energies of rocks to microcracks generated in large numbers throughout the highly stressed region surrounding the crack tip. The two alternative energy sinks: the main fracture surface and plastic formation derive little support from this study. The detailed measurements of the surface topography at magnifications up to 2000X indicate that the total surface area is about 11x the projected area of fracture. Even though this factor is larger than values of 1.5 to 3* and 1.8 to 4 that have been measured by Friedman, et al[11], for several rocks and estimated by Wiederhorn[18] from geometrical considerations, it is not large enough to account for the fracture energy. Note that the measured cleavage fracture energy of calcite at -196°C is 0.46 J/m^2[9]; 11 times this value is still only $\sim 3\%$ of the R-value of the sandstone at this temperature. There is also little basis for believing that the small crystallites in the calcite cement of the limestone and the sandstone are more likely to dissipate fracture energy by undergoing plastic deformation at -196°C than the massive crystal tested by Gilman. For one thing, the isolated crystals extracted from the fracture produced at room temperature displayed no dislocations when viewed in transmission. The fact that the appearance of the fracture calcite cement is exceedingly granular in the limestone (see Figure 8) implies that the crystallite boundaries are weaker than the cleavage plane, that dislocation generation is, if anything, less likely, and that the fracture energy (per unit surface area) could be somewhat smaller than the value measured by Gilman. It should also be noted that the contribution of

---

* These numbers are based on examinations at 100X magnification and may be compared with the value 3.7 obtained in this study at 100-magnification.

plastic deformation to the fracture energy of polycrystalline MgO, a so-called ductile ceramic is only 18 J/m^2[19], and would not account for the fracture energies of the rock samples. It thus appears that plastic deformation is not a major energy sink, either at room temperature, or at -196°C. The substantial reduction of the R-value for the sandstone with temperature can be accounted for in terms of internal stresses arising from differential thermal expansion and microcracking as discussed in the next section.

In contrast, microcrack formation is supported by a number of observations of the present study, as well as the work of Moavenzadeh and Kugel[10] and Friedman and coworkers[11]:

(1) <u>Acoustic Emissions</u>. Large amounts of acoustic emissions are detected in Region II, before the extension of the main crack is observed. It is difficult to account for these emissions except as instances of microcracking in the region surrounding the initial slot tip.

(2) <u>Nonlinear Compliance</u>. It was generally found that acoustic activity initiated at about the beginning of nonlinearity in the load-displacement record. The correlation is consistent since the formation of numerous microcracks will reduce the effective elastic modulus of the specimen.

(3) <u>Permeability</u>. The increased permeability to the epoxy resin in the sandstone is another indicator of extensive cracking adjacent to the initial slop tip and main fracture path. Increases in permeation rate by a factor of two to three are suggested by the resin penetration distances shown in Figure 10. It should be noted that this specimen was impregnated under zero load and some microcracks will be partially or completely closed, therefore, this permeability increase is lower than might be expected under load.

(4) <u>X-Ray Studies</u>. Friedman and coworkers[11] demonstrate a relaxation of residual elastic strains both in the quartz grains of Tennessee sandstone in a zone as deep as 5 mm adjacent to the fracture surface of broken bend specimens and in the quartzite. Such relaxations are believed to be the result of rupture of the interconnecting calcite cement.

(5) <u>Direct Observation</u>. Quantitative measurements by optical microscopy by Moavenzadeh and Kugel[10] show that the crack area contains numerous microcracks adjacent to the main crack in broken concrete specimens equivalent to as much area as 20 times the cross-sectional area of their specimens. Microcracking at the grain boundaries of Chichowee quartzite has also been revealed by Friedman and coworkers[11] with a silver nitrate staining technique.

Additional evidence that the extent and frequency of the microcracking is consistent with the observed R-values is derived from the compliance measurements. This is done by assuming that the point of deviation from linearity in the load-displacement record is coincident with the onset of extensive microcracking, and by estimating the total area of microcracks on this basis. From a analysis developed in Appendix B we estimate the total surface area associated with freshly produced* microcracks in a DCB specimen as

$$A = \frac{b^2 h}{4\pi\alpha} [a - \frac{S}{4} + \frac{S}{3} \ln \frac{3(S-2a)}{2S} + \frac{S^2}{18(S-2a)}]$$

where

$$S = \frac{h^2 b \sigma_c}{P}$$

(3)

---

* Equation (3) does not contain the area of preexisting voids and cracks.

a   =   slot length in the specimen

h   =   beam height (one-half total width)

b   =   specimen thickness

α =   average area per microcrack

σ_c =   average critical tensile stress required to crack the calcite

P   =   applied load.

Equation (3) is obtained by approximating the DCB specimen by two cantilever beams anchored to a rigid foundation. This approximation is quite adequate in view of two other assumptions, namely: (a) the microcracks are noninteracting and (b) σ_c is the maximum tensile stress which can be supported by the rock. Denoting the bracketed term on the right side of Equation (3) as F, average values of F obtained at maximum load in tests of three limestone specimens and of six sandstone specimens are given in Table III.

TABLE III. ESTIMATED TOTAL MICROCRACK SURFACE AREAS

Rock	Estimated Single Microcrack Area (α)-m^2	Average F at Max. Load-m	Total Microcrack Area at Max. Load from Eq. 3 m^2
Limestone	10^{-6}	3.0×10^{-3}	0.154
Sandstone	10^{-7}	5.4×10^{-3}	2.76

The microcrack size was estimated on the basis that, when first formed, the area of each microcrack will be approximately equal to the particle cross-sectional area. The results indicate that at maximum load, when gross crack extension initiates, the accumulated area of freshly formed microcracks

in the limestone is about 0.15 m^2 and about 2.8 m^2 in the sandstone. While these calculated areas should serve only as rough estimates they certainly indicate that the amount of microcrack area, as computed simply from the loss of compliance of the specimen, is truly very large. By virtue of the inverse dependence of A on α, Equation (3) also predicts that microcracking should be more extensive in the sandstone than in the limestone by about a factor of 10-20. The measured R-values for the sandstone are about 2 to 8 times larger than for the limestone which is in very reasonable agreement with the prediction of Equation (3) considering the fact that σ_c may be somewhat different in these two rocks. Thus, while the model on which Equation (3) is based is crude (and could certainly be improved), it does give a reasonable account of the observed behavior. Furthermore, it establishes an important link between microstructure and the fracture behavior of rocks.

The conceptual picture describing the development of microcracks at the tip of a machined slot in these two rock materials is summarized schematically in Figure 14. Point (a) corresponds to the unloaded conditions. A few fresh microcracks introduced during cutting surround the slot. As the load is applied, some cracking occurs on the weakest planes very near the slot tip as in (b). At this point too few microcracks have formed to produce a detectable nonlinearity in the load-displacement record and they formed at stresses too small to produce an acoustic signal of detectable amplitude. With further increases in load the microcracked region becomes larger and stronger interfaces and linkages rupture producing a much more intensely cracked volume surrounding the slot tip as envisaged in (c). The loading record is now nonlinear (Region II) and the rupture of the interfaces at these load slot tip stress levels produces detectable acoustic signals. There may

48
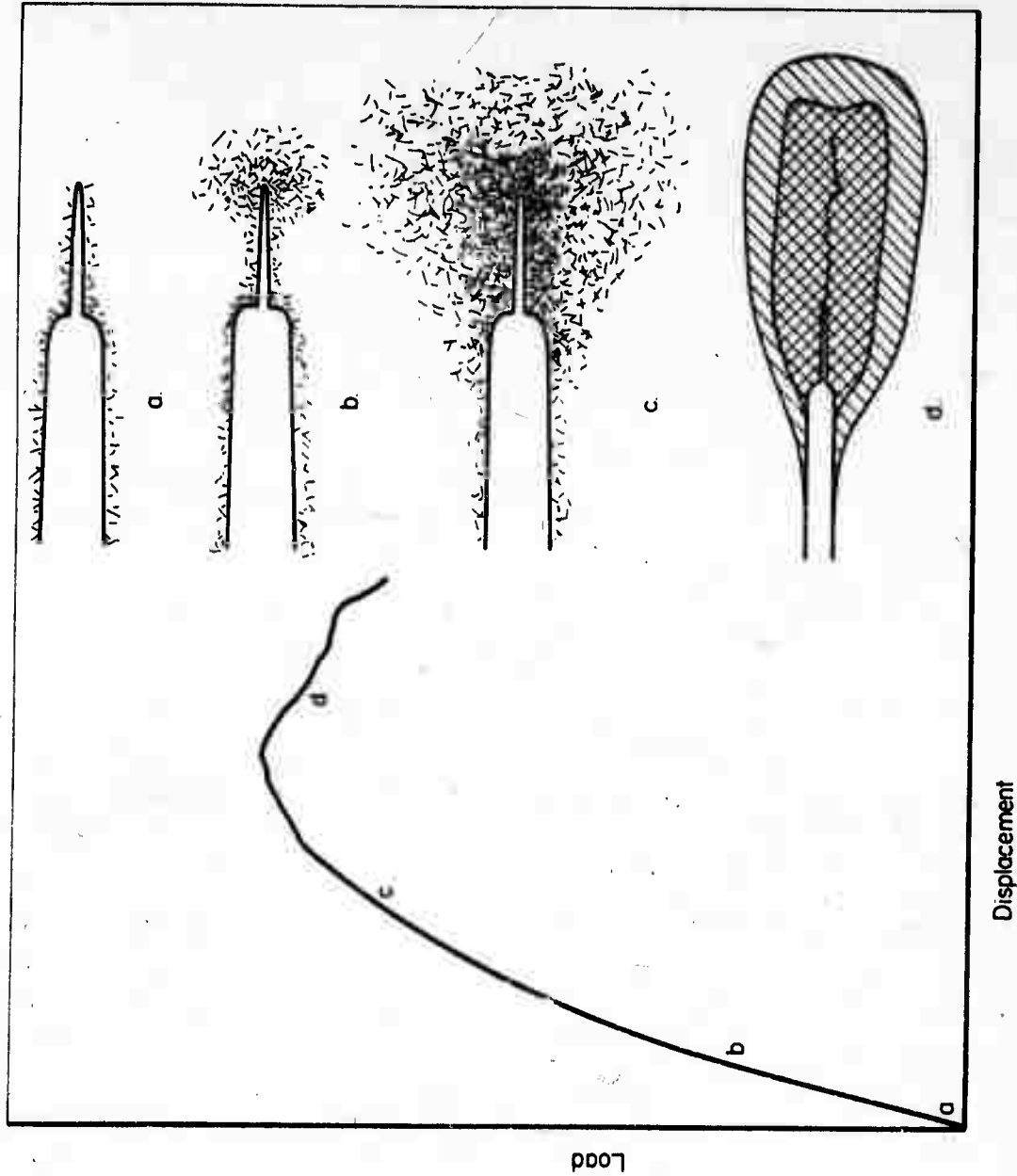
FIGURE 14. A SCHEMATIC REPRESENTATION OF THE STAGES OF DEVELOPMENT OF A DAMAGE ZONE AROUND A MACHINED SLOT IN ROCK. Initially only a few fresh microcracks are present as in (a). On loading the rock first responds elastically corresponding to Region I and only a few microcracks are produced on weakest interfaces,(b). Then in (c) the damage has become intesnse and spreads rapidly leading to inelastic behavior as in Region II. Finally, the Region III behavior is shown at (d) where the main crack and the damage zone extend together.

be locations along the leading edge of the slot where some microcracks have linked together and have in turn joined the slot tip. However, it seems more appropriate to simply refer to this region as a zone of damage which is still capable of supporting load and, therefore, the conditions for extension of the main crack are still unsatisfied. Further increases in load extends the damage zone somewhat, but at the slot tip rupture of the remaining strongest linkages occurs and gross crack extension begins at about the point of maximum load (onset of Region III). At this stage expansion of the damage zone may still be more rapid than the growth of the main crack. This is suggested by the observation that R increases in the initial stages of crack extension. Finally, however, the rate of propagation of the main crack tip becomes equal to the rate of growth of the damage zone extending ahead of the crack tip. Thus, a steady-state situation is achieved in which the main crack extends, pushing the damage zone ahead of it at the same rate as is depicted in (d). R becomes equal to the asymptotic limit determined by the size of the damage region and the rate of microcrack production within it. Inherent in this model is the supposition that the various interfaces which act as potential microcrack sites exhibit a broad range of load-carrying capability. If each of these interfaces could support the same tensile load, microcracking would be confined to the slot tip and the development of a large, energy-absorbing damage zone prior to the growth of the main crack would not be possible. It is interesting to note that similar concepts and the substitution of crazed regions for microcracks have recently been elaborated on by Hull, et al[20,21], to explain the toughness of glassy polymers.

As pointed out by Perkins and Bartlett[8] one commonly finds a large discrepancy between the measured tensile strength of rocks and the theoretical tensile strength based on a simple Griffith theory and measured R-values. As

an example, if the rock contains cracks of length (or diameter for penny-shaped cracks), 2a, oriented perpendicular to an applied uniaxial stress then the tensile strength is

$$\sigma_t = \beta \sqrt{\frac{ER}{\pi a}} \quad , \tag{4}$$

where β is a geometry dependent constant of order unity. Table IV compares measured tensile strengths with calculated values based on R-measurements on the same materials. It shows that measured values of strength fall far below the predicted levels.

The conceptual picture of the zone of damage described above offers a possible explanation for this discrepancy. This zone, while providing a means of dissipating large amounts of energy, also serves another very important function. The formation of numerous microcracks in this zone diminishes the stress concentration at the tip of the main crack or slot. The consequences of this process are precisely the same as in a metal in which a plastic zone developes in response to large stresses at the crack tip. A typical relation between fracture stress and crack size for a metal is represented in Figure 15. For long crack lengths the fracture stress varies with crack length in a manner described by Equation (4) since the R associated with onset of rapid crack extension is a material property and, hence, constant. However, Equation (4) only applies as long as the size of the plastic zone is small relative to the dimensions of the structure. As the crack size is reduced the fracture stress increases until it approaches the yield strength and wide-spread plastic deformation of the structure occurs prior to fracture. Equation (4), which is based on a linear elastic analysis, no longer applies and fracture stress levels out and becomes equal to the unnotched fracture stress as the flaw size is reduced to zero. Because the damage zone has an effect on the slot crack tip stress field which is quantitatively similar to

TABLE IV.   COMPARISON OF MEASURED TENSILE STRENGTH OF SEVERAL LIMESTONES
WITH VALUES CALCULATED FROM THE GRIFFITH THEORY
(Data of Perkins and Bartlett)

Limestones	Young's Modulus GN/m^2	Fracture Energy R, J/m^2	Tensile Strength, MN/m^2	
			Measured, MN/m^2	Calculated*, MN/m^2
Austin	11.0	14.0	1.81	7.0
Carthage	32.4	77.0	4.68	28.2
Lueders	19.3	38.5	4.11	15.4
Indiana	19.3	84.0	3.58	22.7

*   Assuming a critical flaw size of 1 mm.
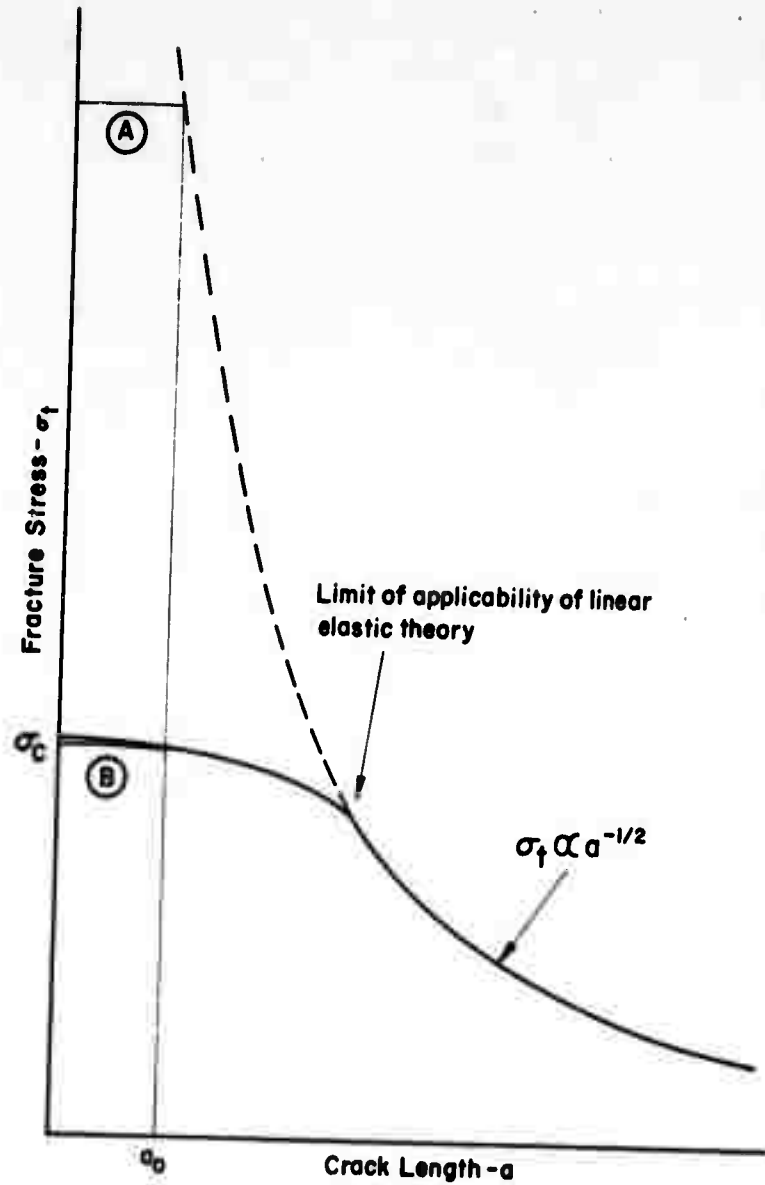
FIGURE 15. THE GENERAL RELATION BETWEEN FRACTURE STRESS AND CRACK LENGTH IN
MATERIALS CAPABLE OF INELASTIC RELAXATIONS AT THE CRACK TIP. For
large crack lengths Equation (4) applies. For small crack lengths,
as at a_o, inelastic deformation becomes predominant and the dis-
crepancy between the predicted fracture stress, at Ⓐ, and the
measured fracture stress, at Ⓑ, can be quite large.

that of a plastic zone, we can also expect a very similar crack length-fracture stress relation in rocks. Thus, if a rock sample contains a small flaw, a large portion of the rock will undergo microcracking before the stress on the rock is sufficient to extend the flaw. In such a case a description of the critical condition for crack extension must take these inelastic processes into account. The use of Equation (4), for example, to compute R from the unnotched tensile strength and an assumed flaw size, say, a_o, characteristic of the microstructure of the rock, presupposes a fracture stress-flaw size relation as indicated by the dashed line in Figure 14. The result is a gross underestimate of the true R.

An important consequence of this argument is the expectation that R-values of rocks, like the toughness values of ductile metals, are systematically underestimated and display a flaw- and specimen-size dependence when these dimensions are relatively small, e.g., when

$$D \geq C \ E \ R/\sigma_c^{\ 2} \quad , \tag{5}$$

where D is the limiting specimen dimension, C is a constant of order 0.5 to 2 depending on the specimen geometry, and σ_c is the stress at which micro-crack generation becomes significant, i.e., the tensile strength of an un-notched test bar. The critical specimen dimensions are usually the specimen width in the case of tensile specimens or the beam height in the case of a DCB and notch bend specimen. For values of E, R, and σ_c typical for limestone $D \sim 10$ cm indicating that the size of our specimens may have been too small to measure the size-independent value of R. This size effect is distinct from that associated with Weibull-type distributions of flaws or other microstructural entities, and could account for the lower R-value reported by Friedman and coworkers for limestone (see Table II).

It should be apparent that the microcrack-zone of damage concept offers new opportunities for explaining the mechanical behavior of brittle materials. In the case of rocks it makes it possible to rationalize:

(1) The discrepancy between R and surface energy

(2) The discrepancy between measured and calculated unnotched strength values

(3) The lack of a correlation between fracture energy and unnotched strength values among different types of rocks and ceramic materials

(4) A wide range of microstructural effects

(5) Size effects and

(6) The apparent insensitivity of R to notch root radius.

Since the fracture energies of some ceramics approach those of rocks, the microcrack-zone of damage approach may also be of some value for interpreting and modifying the strength and toughness or this class of materials.

REFERENCES

(1) H. R. Pratt, W. S. Brown, and W. F. Brace: Dynamic Crack Mechanics, G. B. Clark, ed. AIME (New York) (1971) p. 27.

(2) P. L. Gutshall and G. E. Gross: Eng. Fract. Mech. 1 463 (1969).

(3) R. W. Davidge and G. Tappin: Proc. Brit. Ceram. Soc. 15 47 (1970).

(4) D. B. Binns and P. Popper: Proc. Brit. Ceramic Soc. 6 71 (1966).

(5) H. G. Tattersall and G. Tappin: J. Mat. Sci. 1 296 (1966).

(6) A. G. Evans and R. W. Davidge: J. Mat. Sci. 5 314 (1970).

(7) A. G. Evans and R. W. Davidge: Phil. Mag. 20 373 (1969).

(8) T. K. Perkins and L. E. Bartlett: Soc. Pet. Eng. J., (1963) p. 307.

(9) J. J. Gilman: J. Appl. Phys. 31 (1960) p. 2208.

(10) F. Moavenzadeh and R. Kuguel: J. of Materials 4 (1969) p. 497-519.

(11) M. Friedman, J. Handin, and G. Alani: Technical Report No. 4 to Dept. of the Army, Texas A&M Univ., College Station, Texas, Sept. 15, 1971.

(12) R. G. Hoagland, A. R. Rosenfield, and G. T. Hahn: Met. Trans. 3 123 (1972).

(13) H. R. Hardy and Y. S. Kim: Proceedings of the Twelfth Symposium on Rock Mechanics, AIME, (1971) p. 301.

(14) P. La Mori, Battelle-Columbus, Private Communication (1972).

(15) T. K. Perkins and W. W. Krech: Soc. Petroleum Eng. J. 237, (1966) p. 308-314.

(16) J. Handin, R. V. Hager, Jr., M. Friedman, and J. N. Feather: Bull. Am. Assoc. Pet. Geol. 47 (1963) p. 717.

(17) K. T. Kirkpatrick and C. H. Summerson: Ohio J. of Science, March, 1971, p. 106.

(18) S. M. Wiederhorn: NBS Spec. Publ. 303 217 (1968).

(19) A. G. Evans: Phil. Mag. 22 (1970) p. 841.

(20) J. Murray and D. Hull: J. Polymer Sci. [A2] 8 1321 (1970).

(21) M. Bevis and D. Hull: J. Math. Sci. 5 983 (1970).

(22) D. Hull: J. Matl. Sci. $\underline{5}$ 357 (1970).

(23) M. F. Kanninen: "An Augmented Double Cantilever Beam Model for Studying
      Crack Propagation and Arrest", submitted to Intl. J. of Frac. Mech.

(24) R. G. Hoagland: Trans. ASME $\underline{89}$, series D (1967) p. 525.

APPENDIX A

Computation of Energy Dissipation Rates

At the basis of the Griffith energy balance or thermodynamic approach to fracture is the calculation of the stored elastic strain energy in the body given by

$$U = \int_{\tau} \left(\int \sigma_{ij} \, d\epsilon_{ij} \right) d\tau \qquad (A-1)$$

Here ϵ denotes elastic strain and σ the stress. The subscripts follow the Einstein tensor notation. The outer integral, τ, denotes integration over the volume of the body. The evaluation of U is greatly simplified if there exists a linear (Hookeian) relation between stress and strain throughout the body. Further, the elastic moduli are assumed constant throughout and that the material remains compatible (i.e., no cracks or voids develop).

This latter assumption is apparently violated to various degrees in rocks subject to tensile stresses. As a consequence of forming or opening many small cracks, the material becomes more compliant. Equivalently, the bulk elastic properties appear to be reduced. However, within the framework of these assumptions, we can obtain in the case of a DCB specimen, a simple relation between the component of force perpendicular to the crack, P, and displacement, y (between the points of load application):

$$y = \frac{\phi P}{Eb} \qquad (A-2)$$

where E is Young's modulus, b is specimen thickness, and ϕ is the compliance which depends only on the specimen dimensions in the plane perpendicular to the thickness and crack length. The stored elastic strain energy also simplifies to

$$U = \frac{1}{2} Py \tag{A-3}$$

and substituting from Equation (A-2)

$$U = \frac{Eby^2}{2\phi} \tag{A-4}$$

The stored elastic energy decreases as the crack extends at a rate given by

$$G = -\frac{1}{b} \frac{\partial U}{\partial a}$$

or

$$G = \frac{E}{2} \left(\frac{y}{\phi}\right)^2 \frac{\partial \phi}{\partial a} \tag{A-5}$$

where G is the elastic energy release rate. If the stored elastic energy is released at the same rate as it is dissipated then $G = R$ and Equation (A-5) is the means of calculating R provided ϕ can be related to crack length. Kanninen[8] has derived this relation and obtains

$$\Phi = \frac{2}{\lambda^3 h^3} \left[2\lambda^3 a^3 + 6\lambda^2 a^2 \left(\frac{\text{Sinh } \lambda c \text{ Cosh } \lambda c + \sin \lambda c \cos \lambda c}{\text{Sinh}^2 \lambda c - \sin^2 \lambda c}\right) + \right.$$

$$\left. + 6 \lambda a \left(\frac{\text{Sinh}^2 \lambda c + \sin^2 \lambda c}{\text{Sinh}^2 \lambda c - \sin^2 \lambda c}\right) + 3 \left(\frac{\text{Sinh } \lambda c \text{ Cosh } \lambda c - \sin \lambda c \cos \lambda c}{\text{Sinh}^2 \lambda c - \sin^2 \lambda c}\right)\right] \tag{A-6}$$

$$\lambda = \frac{(6)^{1/4}}{h}$$

$$c = L - a$$

where h is the beam height (one-half the width of the specimen) and L is the specimen length.

Substituting Equation (A-6) into (A-5) gives a means of determining R in terms of the measured displacement y and crack length, a. The displacement is measured at the end of the steel pin blocks (cf., Figure 1). Since the pin blocks have negligible compliance compared to the rock, the point of load application is taken as the interface between the end of the specimen and the pin blocks. The measured displacement is corrected to correspond to the displacement at this point.

As the crack extension was often difficult to measure, the crack length could be obtained indirectly based on the assumption that the coefficient of friction between the wedge and pins remained essentially constant during the test. We have $P = \left(\frac{\psi}{\phi}\right)_0 F$ where ψ is the compliance relating y to F, the force applied to the wedge, and the above assumption permits us to set $\left(\psi/\phi\right)_0$ constant. This ratio is obtained at the beginning of the test from the slope of the linear portion of the F-y curve (cf., Figure 2) and ϕ which is calculated from Equation (A-6) using the initial slot length. For other values of y and F, the compliance, ϕ, and crack length can be obtained from the following combination of equations:

$$\phi = \left(\frac{\phi}{\psi}\right)_0 \frac{y}{F}$$

and

$$\phi = Aa^n \tag{A-7}$$

where A and n are constants. Equation (A-7) is empirical but has been shown to provide a good correlation between the compliance and crack length.[9] The constants A and n are obtained from a least squares fit of Equation (A-6) to Equation (A-7).

APPENDIX B

Estimation of Total Microcrack Area

Referring to Figure B-1 we can estimate the effect of a regular array of microcracks on the effective Young's modulus of a material by assuming that the cracks are noninteracting, i.e., they are sufficiently far apart that the stress field around any crack is essentially independent of the presence of neighboring cracks. The compliance of a rectangular plate of dimensions ℓ x w and containing one crack of length 2a is given approximately by

$$\phi = \frac{\ell}{Ebw} \left(1 + \frac{\pi a^2}{\ell w}\right) \tag{B-1}$$

where b is the thickness. If we now assemble a plate of dimensions L x W from these singly cracked plates, the compliance of the assembly becomes

$$\Phi = \frac{L}{EbW} \left(1 + \frac{\rho \pi \alpha^2}{b}\right) \tag{B-2}$$

In Equation (B-2), ρ is the number of microcracks per unit volume given by $\rho = 1/w\ell b$ and $\alpha = ba$, the area per microcrack. Equation (B-2) is strictly applicable only to through-the-thickness cracks but for the sake of simplification, we apply it to the case of a three-dimensional array of microcracks each completely embedded. Therefore, by comparison with the compliance of an uncracked plate we obtain

$$E_{eff} \cong \frac{E}{1 + \frac{\rho \pi \alpha^2}{b}} \tag{B-3}$$

for the effective Young's modulus of a solid containing imbedded microcracks.

For a DCB specimen under load it can be recognized that if the load is sufficiently large to produce microcracking E_{eff} will vary throughout the

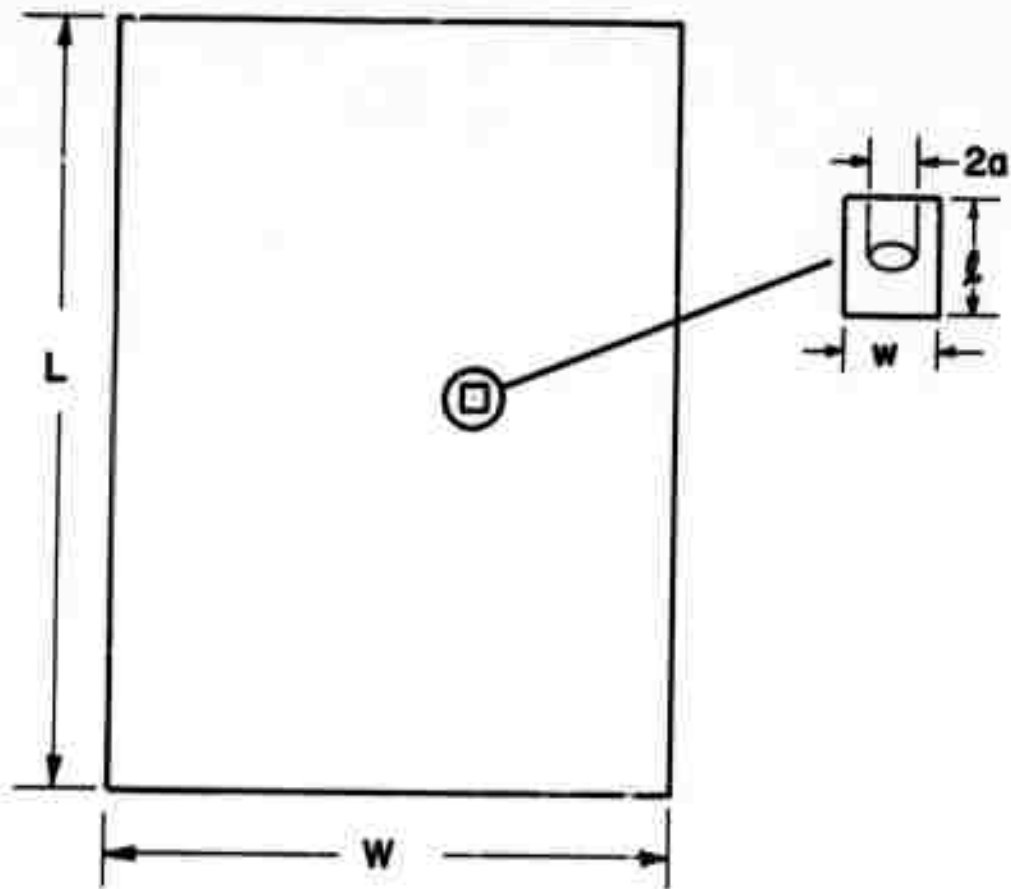FIGURE B-1. THE MODEL USED TO PREDICT THE EFFECT OF FLAW DENSITY ON COMPLIANCE. The plate of dimension L x W is composed of elements of dimension l x w each containing a crack of length 2a.

specimen being smallest near the main crack tip where the microcrack density, and, hence, ρ, is the greatest. To establish a reasonable distribution of microcracks in the specimen we make the assumption that the rock has a constant failure stress, σ_c, i.e., microcracking begins when the tensile stress is increased to σ_c but can become no larger than σ_c. This assumption allows us to define the size and shape of the damage zone. A further simplification is obtained by considering the DCB specimen as two cantilever beams attached to a rigid foundation. Therefore, as each beam is loaded they first behave perfectly elastic until σ_c is reached at the point of maximum stress on the tensile side of the beam. At any stage in the growth of the damage zone we can deduce, from application of inelastic beam theory, that the effective Young's modulus at any point within the damage zone

$$E_{eff} = \frac{9Eh(\frac{1}{2} - \frac{a-x}{S})^2}{9h(\frac{1}{2} - \frac{a-x}{S})^2 + 2(\zeta - y)} \tag{B-4}$$

where $\qquad S = h^2 b\sigma_c/P$

x = coordinate along the length of the beam measured from the foundation*

y = coordinate perpendicular to x and measured from the tensile fiber of the beam*

ζ = the value of y at the damage zone boundary.

Comparing Equations (B-4) and (B-3) indicates that

$$\frac{\rho\pi\alpha^2}{b} = \frac{2(\zeta - y)}{9h(\frac{1}{2} - \frac{a-x}{S})^2} \tag{B-5}$$

---

* The extent of the damage zone is given by $0 \leq x \leq a - \frac{S}{6}$ and $0 \leq y \leq \zeta$ where $\zeta = \frac{3h(a-x)}{S} - \frac{h}{2}$.

If we note that the term $\rho\alpha$ is the amount of microcrack area per unit volume, then the total microcrack area in the damage zone, A, is obtained by integrating the right side of Equation (B-5) over the volume of the damage zone giving

$$A = \frac{b^2 h}{4\pi\alpha} \left[a - \frac{S}{4} + \frac{S}{3} \ln \frac{3(S-2a)}{2S} + \frac{S^2}{18(S-2a)} \right] \, . \qquad (B-6)$$